

Developing an Insect Odorant Receptor Bioelectronic Nose for Vapour-Phase Detection

by Eddyn Oswald Perkins Treacher

A thesis submitted in partial fulfilment of the
requirements of the degree of
Doctor of Philosophy in Physics
School of Physical and Chemical Sciences
Te Herenga Waka - Victoria University of Wellington

Nov 2024



Abstract

The ability to detect volatile organic compounds in a highly sensitive and selective manner is desirable for applications as varied as diagnosis of illnesses at a remote clinic, monitoring of air in an industrial setting, or identification of invasive organisms at a biosecurity checkpoint. Historically, animal noses have been used for such tasks, as their combined sensitivity and selectivity are superior to traditional artificial sensors. However, training and deploying animals in such situations is both time and cost intensive. In recent years, an improved understanding of *in vivo* biological sensing has driven efforts to mimic these highly efficient processes in an artificial sensor format.

To this end, a “bioelectronic nose” was developed. This sensor uses an artificial transducer to amplify responses of an insect odorant receptor protein to specific volatile compounds. Thin-film transistors were used as the amplifier element, given their low cost, small size and extreme sensitivity. Various thin-film morphologies were compared, and their suitability for bioelectronic nose development assessed. Transducers made using a novel steam-assisted thin-film deposition technique were found to have highly consistent device-to-device electrical properties relative to other films. Films made using this process typically showed more surface contamination than other morphologies, but their high sensitivity was nonetheless confirmed with a non-specific sensing series in an aqueous environment.

One of the major challenges encountered in this thesis was variability in the quality of sensor functionalisation. Raman spectroscopy and fluorescence microscopy confirmed an existing non-covalent attachment method could successfully immobilise nanodiscs onto the transistor channel region. However, various sensors functionalised using the same procedure often exhibited no sensing activity. Extensive electrical characterisation indicated the presence of an unidentified contamination layer preventing electrical interaction between the insect odorant receptors and transducer thin-film. It was shown that this layer was unlikely to be directly associated with the thin-film morphology used for the transducer.

Subsequently, an alternative biotin-based non-covalent method was used for functionalisation of the proteins, which eliminated several possible contamination sources. This alternative biotin-based method was used to demonstrate successful aqueous sensing of femtomolar concentrations of methyl salicylate by an iOR10a-functionalised device. When tested in a custom-built vapour delivery system, a similar bioelectronic sensor was shown to be highly sensitive to the target vapour. However, consistent reproduction of the biotin-based method was challenging due to the harsh cleaning method involved. It was therefore difficult to determine conclusively whether sensor responses were selective. By finding new, systematic approaches to address the major barriers to sensor success carefully identified in this work, there are promising signs that a highly reliable vapour-phase bioelectronic nose can be produced.

Acknowledgements

I would first like to acknowledge the lands of my ancestors, and the lands of the sovereign first peoples to which my ancestors travelled. We each come from the land, live off the land and return to the land.

Noon of Essex to Warrang, on the Friends, Autumn 1811

Cave of Cambridgeshire to Warrang, on the Royal Charlotte, Autumn 1825

Boyce of Suffolk to Warrang, 1832

Charlton of Northumberland to Warrang, on the Clyde, Spring 1834

Prouse of Devonshire to Pito-one, on the Duke of Roxburgh, Summer 1840

Ebden of Devonshire to Pito-one, on the Tyne, Winter 1841

Collis of Hampshire to Pito-one, on the Birman, Autumn 1842

Swann of Loch Garman to Te Whanganui-a-Tara, 1844

Blythe of Berkshire to Whakatū, circa 1846

Innes of Berkshire to Naarm, on the Sacramento, Autumn 1853

Sheppard of Gloucestershire to Naarm, 1853

Bruce of London to Naarm, on the Omega, Autumn 1855

Quennell of Surrey to Warrang, on the Asiatic, Winter 1855

Barr of Glasgow to Kōpūtai, on the Sir Edward Paget, Winter 1856

Perkins of London to Te Whanganui-a-Tara, on the Matoaka, Spring 1859

McKee of Antrim to Tāmaki Makaurau, on the Indian Empire, Spring 1862

Sandilands of Peeblesshire to Ōtepoti, circa 1864

Treacher of Berkshire to Te Whanganui-a-Tara, on the Wild Duck, Summer 1865

McTaggart of Argyllshire to Kōpūtai, on the Edward P. Bouvierie, Autumn 1869

Chapman of Kent to Whakatū, on the Adamant, Winter 1874

Cheel of London to Whakatū, on the Queen Bee, Winter 1877

Hutchison of Aberdeen to Tarntanya, before 1882.

I chose to start my doctoral studies just a few months into a global pandemic. Completing a challenging project with a worldwide crisis in the background might have been impossible without the supervision of AProf. Natalie Plank. Her ability to adapt to and overcome any problem has taught me that there is no situation which is truly unmanageable. I am deeply grateful for her leadership throughout a time of particular chaos.

Acknowledgements

I started this project with minimal formal training in biological science, coming from a primarily physics and engineering background.

The immense support I received from Melissa Jordan and Colm Carraher from the Institute for Plant and Food Research (PFR) to complete this project meant that this was not an issue, and I thank them both immensely for this.

I would not have been able to begin this thesis without the financial backing and support I received from PFR and the Better Border Biosecurity (B3) programme. In particular, I am very grateful to Andrew Kralicek, formerly with PFR and now at Scentian Bio, and the ex-Director of B3, David Teulon, for helping to secure funding for my project. I would also like to thank the donor of the Ernest Marsden Scholarship in Physics for their significant financial support.

There are many incredibly supportive people who I worked alongside during my project. I would like to start off by thanking Rifat Ullah, whose mentoring and kindness encouraged me to pursue further study. His work on the initial design and setup of the vapour delivery system was invaluable to me throughout this project. I am also especially grateful to Alex Puglisi, for constructing the mechanical elements of the vapour delivery system and giving me extensive feedback on the system design. I would like to thank Peter Coard, for his advice and guidance when constructing the electrical elements of the vapour delivery system. I thank Selvan Murugathas, too, for his advice on constructing the insect odorant receptor sensors, as well as Damon Colbert and Valentina Lucarelli, who provided the insect odorant receptor nanodiscs used in this work.

Thank you to AProf. Ben Ruck, my supportive secondary supervisor, and to AProf. Franck Natali, for always asking about my thesis in the tearoom. Thank you to Gideon Gouws for his friendly encouragement and advice. For their substantial technical assistance and mentoring during this project, I thank Alan Rennie, Grant Franklin, Chris Lepper, Rashika Gunasekara, Pete Jebson and Sushila Pillai from VUW, Andrew Chan from PFR, AProf. Charles Unsworth from the University of Auckland, and Prof. Simon Brown and his nanomaterials group from the University of Canterbury.

I was lucky enough to start my doctoral program just as a group of supportive and talented senior students were finishing, and finished just as a group of enthusiastic and talented new doctoral students were starting. A special thanks to Jenna Nyugen, Erica Happe and Erica Cassie for teaching me the fabrication processes and characterisation procedures that made this thesis happen; and a special thanks to Marissa Dierkes, Danica Fontein, Sangar Begzaad and Alireza Zare, for their incredible support throughout the thesis writing process. I am also thankful for the assistance of the cleanroom group interns over the course of my PhD, including Liam, Hayden and Lotte. I would further like to thank everyone else I shared an office with and worked alongside, including Jackson, Will, Roshni, Ali, Kira, Catherine, Martin, Janani, Ted, Kiri and Joe.

A massive thank you to Openstar Technologies. It has been an honour to work on a cutting-edge plasma physics project right here in Te Whanganui-a-Tara. A particularly big thank you to Ratu, Darren, Thomas and Craig for having me as part of the

Acknowledgements

plasma physics team. Thank you also to the other Openstar interns, in particular the other plasma physics interns, Valentina, Benji and Chris. I wish you success in all your dipole-confined plasma related endeavours.

I want to thank Shodokan Aikido New Zealand for their support throughout this thesis, in particular for the once-in-a-lifetime opportunity to travel to Osaka to be graded for first-dan by Nariyama Shihan. Thanks for all the training and support, Ian. Thank you to all the friends and family, old and new, who have supported me over these wild past few years. You know who you are.

Thank you to my brother, Keeson, and to my parents, Hilary and Phillip. Your support means everything to me, and I would not be where I am today without you. Our Friday lunchtime cafe visits inspired and motivated me throughout the doctoral program. Thank you, thank you, thank you for your love, your compassion, and for being there for me.

Finally, thank you Nina. Your love has kept me going through the most difficult and most wonderful times over the last three and a half years. You are the light of my life, and I am so happy to have taken on this challenge with you by my side.

Arohanui and peace to you all, Eddyn (Ned)

Table of Contents

Abstract	i
Acknowledgements	iii
Table of Contents	vii
List of Figures	xi
List of Tables	xiii
List of Abbreviations	xv
1. Introduction	1
1.1. Background	1
1.2. Thesis Outline	2
2. Characteristics of Pristine Carbon Nanotube & Graphene Field Effect Transistors	5
2.1. Introduction	5
2.2. Carbon Nanotube Network Morphology and Composition	6
2.2.1. Atomic Force Microscopy	6
2.2.2. Raman Spectroscopy	15
2.3. Electrical Characteristics of Pristine Devices	17
2.3.1. Python Analysis	17
2.3.2. Graphene Devices	19
2.3.3. Carbon Nanotube Network Devices	20
2.4. Aqueous Sensing of Phosphate Buffered Saline Concentration	25
2.4.1. Control Series and Baseline Drift	25
2.4.2. Sensing Series	27
2.5. Conclusion	29
Appendices	39
A. Vapour System Hardware	39
B. Python Code for Data Analysis	41
B.1. Code Repository	41

Table of Contents

B.2. Atomic Force Microscope Histogram Analysis	41
B.3. Raman Spectroscopy Analysis	41
B.4. Field-Effect Transistor Analysis	41
References	43

List of Figures

2.1. 2.5 $\mu\text{m} \times 2.5 \mu\text{m}$ atomic force microscope (AFM) images of carbon nanotube films deposited using various methods, shown side-by-side with histogram height distributions and kernel density estimate (KDE) plots corresponding to each image. The network shown in (a) with height distribution shown in (b) was deposited in solvent, the network shown in (c) with height distribution shown in (d) was dropcast in surfactant, and the network shown in (e) with height distribution shown in (f) was dropcast in surfactant with steam present.	7
2.2. 2.5 $\mu\text{m} \times 2.5 \mu\text{m}$ atomic force microscope (AFM) images of SiO_2 substrates alongside histogram height distributions and KDE plots corresponding to each image. The substrate in (a) and (b) was exposed to solvent, the substrate in (c) and (d) was exposed to surfactant, and the substrate in (e) and (f) was exposed to surfactant with steam present. The inset in (f) shows a close-up view of the long tail of the distribution.	8
2.3. A mask, shaded green, sets a height threshold so that masked features are hidden from the height dataset. The network in (a), (c) and (e) was solvent-deposited, while the network in (b), (d) and (f) was surfactant-deposited. The maximum substrate height of each network is masked in (a) and (b), the median background height is masked in (c) and (d), while outlier artifacts have been masked in (e) and (f).	10
2.4. Histogram height distributions for each carbon nanotube network with corresponding kernel density estimate plots collected via the morphology analysis method outlined by Vobornik <i>et al.</i> [39]. The histogram for the solvent-deposited network in (a) is shown in (b) and the histogram for the surfactant-deposited network in (c) is shown in (d). The red dotted line represents the lower bound for multi-tube bundles at 2.9 nm, assuming the minimum nanotube diameter is 1.45 nm.	11
2.5. The dense steam-deposited network is covered with a mask showing the maximum height of the substrate and less-bundled carbon nanotubes in (a), a mask showing the median height of this region in (b), and a mask highlighting imaging artifacts in (c). A histogram of bundle measurements above the maximum height of the substrate is shown in (d).	14

List of Figures

- 2.6. A series of nine Raman spectra at different locations across a 40 $\mu\text{m} \times$ 100 μm carbon nanotube film region, where (a) shows spectra from a film deposited using solvent while (b) shows spectra from a film deposited with surfactant in the presence of steam. (c) shows a histogram of the range of D-peak/G⁺-peak spectral ratios corresponding to each film. 16
- 2.7. A comparison of signal with analyte addition plots taken from a PBS dilution sensing dataset. In (a), a simple difference before and after addition calculation was performed on filtered data with the baseline drift removed, while in (b), baseline drift was not removed before performing the calculation. 18
- 2.8. These figures show liquid-gated transfer characteristics of channels from two AZ® 1518 encapsulated graphene devices. The characteristics of working device channels upon initial exposure to 1× PBS are shown in (a) and (b). The transfer characteristics of channel 1 in (a) and channel 5 in (b) after various degrees of exposure to 1× PBS are shown in (c) and (d) respectively, with each transfer sweep numbered in the order the sweeps were taken. The dashed lines correspond to measurements of gate leakage current. 19
- 2.9. Back-gated (left) and liquid-gated (right) transfer characteristics of AZ® 1518 encapsulated field-effect transistors, where the film was deposited with solvent in (a) and (b), deposited with surfactant in (c) and (d), and deposited with surfactant in the presence of steam in (e) and (f). A step size of 100 mV was used for the backgated sweeps in (a), (c) and (e), while a step size of 20 mV was used for the liquid-gated sweeps in (b), (d) and (f). Gate current (leakage current) is shown with a dashed line. The source-drain voltage used for all sweeps was $V_{ds} = 100\text{mV}$, and 1× PBS was used as the buffer for the liquid-gated measurements here. 21
- 2.10. Backgated transfer sweeps were taken of an single unencapsulated device with a 300 nm SiO₂ layer and steam assisted surfactant-deposited carbon nanotube network channels before and after being covered in 50 μL 1× PBS. 22
- 2.11. These boxplots illustrate the statistical distribution of (a) the on-off ratio, (b) the transconductance at $V_g = 0\text{ V}$, (c) the threshold voltage and (d) the subthreshold slope of liquid-gated and AZ® 1518 encapsulated transistor channels fabricated using solvent-deposited, surfactant-deposited or steam-assisted surfactant-deposited methods. For each deposition type, electrical characteristics were taken of 21 channels of at least three separate devices. The boxes indicate the 25th and 75th percentile of the distribution. 32

- | | |
|---|----|
| 2.12. The transfer characteristics in (a) were taken of the steam-deposited carbon nanotube field-effect transistor used here for an example of salt concentration sensing. The absolute values of measurements are shown, so that negative values resulting from measurement error can be visualised. Linear fits to the PBS control series from each channel from 1200 s onwards are shown in (b), while exponential fits to the PBS control series from 0 – 1200 s with the linear fit subtracted are shown in (c). No significant response to PBS additions are seen at any of the addition times from 100 – 600 s. | 33 |
| 2.13. A multiplexed salt concentration sensing series across eight channels of a steam-assisted surfactant-deposited carbon nanotube device. The source-drain voltage V_{ds} was 100 mV, and gate voltage V_g was 0 V. In (a), the raw current measurements for each channel are shown alongside gate current. The same measurements after despiking, removal of baseline drift and normalisation to initial current are shown in (b), (c) shows the data in (b) after being processed with a moving median filter. | 34 |
| 2.14. The signal changes in Figure 2.13 (c) are shown in (a). This signal data is then shown in box plot format in (b) alongside a fit to the median change in signal for each addition, where $R^2 = 0.86$ | 35 |
| 2.15. The processed data shown in Figure 2.13 (b) and Figure 2.13 (c) is normalised to I_0 , but an alternative normalisation can more effectively filter out remaining drift present. This normalisation presents data relative to both I_0 and the final current reading $\$I_{\{f\}}\$$ using the formula $\$(I - I_{\{0\}})/(I_{\{f\}} - I_{\{0\}})\$$. Using this normalisation, the data in Figure 2.13 (b) and Figure 2.13 (c) can be displayed instead as (a) and (b) respectively. (c) shows a magnified version of the step at addition 2 in (a). | 36 |
| 2.16. The transfer characteristics of a single steam-deposited carbon nanotube field-effect transistor channel are shown in (a). V_{gap} is the gate voltage corresponding to the center of the transistor bandgap, found at the minimum of the characteristic curve. The signal-to-noise ratio of the channel response to a deionised water addition after a suitable control series is shown in (b). The blue current trace in (b) was performed gating the device 150 mV away from V_{gap} , while the red current was performed gating the device 200 mV away from V_{gap} | 37 |

List of Tables

2.1.	The first eight optimised ratios of 2D packed circle diameter to encompassing circle diameter, given to 3 s.f. (encompassing circle diameter = d , number of packed circles = n , approximate packed circle diameter = d_n).	12
2.2.	The median of histogram distributions for solvent-deposited and surfactant-deposited carbon nanotube films, alongside rough estimates for the number of nanotubes present per median bundle, the estimated proportion of multi-tube bundles present across the network and the proportion of substrate covered by the nanotubes.	12
2.3.	Average on-off ratio and major Dirac point voltage for AZ® 1518 encapsulated liquid-gated graphene transistor channels at various stages of exposure to 1× PBS. Electrical characteristics were taken of 6 channels total, three channels from each of two devices.	20
2.4.	The coefficients of linear fits to the PBS control series of each channel between 1200 – 1800 s, where c_1 is the gradient and c_2 is the constant term.	26
2.5.	The coefficients of exponential fits to the PBS control series of each channel between 0 – 1200 s, after the linear fit has been subtracted, where I_0 is the gradient and τ is the time constant.	26
2.6.	This table shows the times at which 20 μL additions were made to the PDMS well, with 300 s between each addition. The concentration in the well after each addition and the change in concentration after each addition are also shown. The well contained 80 μL of 1× PBS at 1800 s. The major component in PBS is NaCl, which has a concentration of 137 mM in 1×.	27
A.1.	Major components used in construction of the vapour delivery system described in this thesis.	39

List of Abbreviations

2D	2-Dimensional
Ab	Antibody
AB	Amyl Butyrate
AB-NTA	Na,Na -Bis(carboxymethyl)- <i>L</i> -lysine hydrate
AFM	Atomic Force Microscope/Microscopy
AH	Absolute Humidity
Avi-tag	Avidin-tag
BMIM	1-butyl-3-methylimidazolium bis(trifluoromethylsulfonyl)imide
BWF	Breit-Wigner-Fano
CAD	Computer Aided Design
CNT	Carbon Nanotube
CVD	Chemical Vapour Deposition
Cy3	Cyanine 3
DAN	1,5-diaminonaphthalene
DAQ	Data Acquisition Input/Output Module
DCB	1,2-dichlorobenzene
DI	Deionised
DMF	Dimethylformamide
DMSO	Dimethylsulfoxide
DMT-MM	4-(4,6-dimethoxy-1,3,5-triazin-2-yl)-4-methylmorpholinium chloride
DMMP	Dimethyl Methylphosphonate
DNA	Deoxyribonucleic Acid
E2Hex	<i>trans</i> -2-hexan-1-al
EB	Ethyl Butyrate
EDC	1-Ethyl-3-(3-dimethylaminopropyl)carbodiimide
EDL	Electric Double Layer
EIS	Electrochemical Impedance Spectroscopy
EtHex	Ethyl Hexanoate
EtOH	Ethanol

List of Abbreviations

FET	Field-Effect Transistor
FITC	Fluorescein isothiocyanate
GA	Glutaraldehyde
GFET	Graphene Field-Effect Transistor
GFP	Green Fluorescent Protein
GPCR	G-protein Coupled Receptor
HEK	Human Embryonic Kidney
His-tag	Histidine-tag
hOR	Human Odorant Receptor
HPLC	High-performance Liquid Chromatography
iOR	Insect Odorant Receptor
IPA	Isopropanol
LOD	Limit of Detection
m-CNT	Metallic Carbon Nanotube
MeOH	Methanol
MeSal	Methyl Salicylate
MFC	Mass Flow Controller
mOR	Mouse Odorant Receptor
MOSFET	Metal-Oxide-Semiconductor Field-Effect Transistor
MSP	Membrane Scaffold Protein
MWCNT	Multi-Walled Carbon Nanotube
ND	Nanodisc
NHS	N-Hydroxysuccinimide
NMR	Nuclear Magnetic Resonance
NSB	Non-Specific Binding
NTA	Nitrilotriacetic Acid
OBP	Odorant Binding Protein
OR	Odorant Receptor
ORCO	Odorant Receptor Co-Receptor
PBA	1-Pyrenebutyric Acid
PBASE	1-Pyrenebutanoic Acid N-hydroxysuccinimide Ester
PBS	Phosphate-Buffered Saline

PCB	Printed Circuit Board
PDL	Poly- <i>D</i> -lysine
PDMS	Polydimethylsiloxane
PEG	Polyethylene Glycol
PID	Photoionisation Detector
PLL	Poly- <i>L</i> -lysine
PPB	Pyrene-PEG-Biotin
PPF	Pyrene-PEG-FITC
PPN	Pyrene-PEG-NTA
PPR	Pyrene-PEG-Rhodamine
PTFE	Polytetrafluoroethylene (Teflon TM)
PVC	Polyvinyl chloride
QCM	Quartz Crystal Microbalance
RH	Relative Humidity
RHI	Relative Humidity and Temperature Indicator
RNA	Ribonucleic Acid
SAW	Surface Acoustic Wave
s-CNT	Semiconducting Carbon Nanotube
SEM	Scanning Electron Microscope/Microscopy
SMU	Source Measure Unit
SPR	Surface Plasmon Resonance
Sulfo-NHS	N-hydroxysulfosuccinimide
SWCNT	Single-Walled Carbon Nanotube
TFTFET	Thin-Film Field-Effect Transistor
TMAH	Tetramethylammonium hydroxide
TX	Transfer Characteristics
UV	Ultraviolet
VI	Virtual Instrument
VUAA1	N-(4-Ethylphenyl)-2-[4-ethyl-5-(pyridin-3-yl)-4H-1,2,4-triazol-3-yl]sulfanylacetamide

1. Introduction

1.1. Background

The ‘bioelectronic nose’, an electronic transducer modified with elements of the animal olfactory system, has the potential to allow specific detection of airborne volatile compounds at concentrations as low as parts per trillion [1]–[4]. An ideal transducer platform is the thin-film transistor (TFT) which is particularly portable, simple to use, small and robust [5], [6]. The thin films used in these field-effect transistors (FETs) include carbon nanotube networks and graphene, low-dimensional nanomaterials which are both highly sensitive and biocompatible [7]. The implications of successful development of such a portable and robust bioelectronic nose are significant. Applications could be found in high-importance fields such as biosecurity, medicine, environmental protection and food safety [3], [8]–[10]. For example, it has been demonstrated that it is possible to detect invasive brown marmorated stinkbugs based on their volatile trace [11]. A bioelectronic nose could potentially accomplish this biosecurity task far more cheaply and efficiently than trained sniffer dogs [12]–[14]. There has been rapid progress in the development of bioelectronic noses using carbon nanotube field-effect transistors (CNT FETs) and graphene field-effect transistors (GFETs) over the past 15–20 years [12], [15], [16].

Insect odorant receptors (iORs) enable simple invertebrates, such as the vinegar fruit fly *Drosophila melanogaster*, to distinguish between a huge number of specific volatile compounds [17]–[21]. Within the past five years, a variety of *Drosophila melanogaster* iORs have been successfully coupled with highly sensitive low-dimensional thin-film transistors (TFTs) for specific detection of fruit-like odors in an aqueous environment [22], [23]. iORs have also been used for sensitive and selective volatile detection in a lipid bilayer format, but not in a portable bioelectronic nose format [24]. In this thesis, my aim was to investigate whether a bioelectronic nose capable of odorant detection in a vapour-phase environment could be constructed by coupling iORs with TFTs. Alongside practical applications, development of a vapour-phase bioelectronic nose using iORs may give us a greater understanding of the mechanisms underlying insect olfaction [12]. The transduction mechanism of nanomaterial-based iOR sensors is still unknown, and I hope to shed further light on the biological and electronic processes underpinning this mechanism [23], [25], [26].

1. Introduction

1.2. Thesis Outline

This thesis consists of nine chapters. The first three chapters, including this one, are background chapters introducing the general topics of this thesis. The fourth and fifth chapters are methods chapters, while the next three chapters (sixth, seventh and eighth) describe the results obtained. The ninth chapter concludes the thesis and discusses possible next steps for future research.

Chapter 2 gives a broad description of carbon nanotube and graphene field-effect transistors with a focus on their use in sensing applications. The chapter begins by looking at the general structure and properties of thin-film transistors, where key figures of merit such as transconductance, on-off ratio, gate current and hysteresis are described. Graphene field-effect transistors (GFETs) and carbon nanotube network field-effect transistors (CNT FETs) are then discussed in greater detail. These descriptions include the chemical composition of each nanomaterial, their conduction behaviour and their unique sensor properties when integrated into a field-effect transistor as a thin-film.

Chapter 3 investigates existing odorant receptor-coupled thin-film field-effect transistors in the literature. First, the biological structure of odorant receptors and membrane formats for their protection *in vitro* are discussed. Details are then provided regarding the construction and operation of existing vertebrate odorant receptor TFT biosensors. The structure and function of the insect odorant receptor is then contrasted with the vertebrate odorant receptor, and existing insect odorant receptor TFT biosensors in the literature are discussed. The chapter finishes with a brief discussion of non-specific binding and its role in hindering biosensor activity.

Chapter 4 describes the fabrication of the CNT FET and GFET transducers used in this thesis and the characterisation techniques used to probe their behaviour. The chapter starts with an introduction to photolithography for thin-film transistor device fabrication. Various techniques are described for random deposition of carbon nanotube networks to act as channels for these thin-film transistors. Characterisation techniques described in this chapter include atomic force microscopy (AFM), fluorescence microscopy, Raman spectroscopy and electrical characterisation with various semiconductor device analysers.

Chapter 5 presents the results obtained from the use of characterisation techniques on the pristine GFETs and CNT FETs. Various carbon nanotube (CNT) network morphologies are displayed and analysed. The Raman spectra and electrical device parameters of these CNT network morphologies are then discussed, along with electrical parameters from graphene devices. The sensitivity of a dense CNT network morphology device is then verified in the aqueous phase.

Chapter 6 explores the non-covalent functionalisation of GFETs and CNT FETs with various linker molecules for insect odorant receptor attachment. The linker molecules tested were 1-pyrenebutanoic acid N-hydroxysuccinimide ester (PBASE) and 1-pyrenebutyric acid (PBA) with 1-Ethyl-3-(3-dimethylaminopropyl)carbodiimide

1.2. Thesis Outline

(EDC). Pyrene-NTA and pyrene-biotin were also investigated as other possible linker molecules. The quality of various functionalisation approaches was then explored with various fluorescently-tagged linker molecules and biomolecules. In this process, various potential obstacles to successful biosensor functionalisation were identified.

Chapter 7 maps out progress made towards the creation of an insect odorant receptor functionalised TFT biosensor for use in a vapour-phase environment. Two different approaches are described that gave rise to working aqueous-phase biosensors. The first functionalisation approach, which used PBASE in methanol, led to irreproducible results when biosensing. Possible factors causing the unreliability of this method were then investigated. A second approach was then designed to avoid the malign influence of any identified factors.

Chapter 8 outlines the development of a vapour delivery system for characterisation of the insect odorant receptor functionalised TFT biosensors in a vapour-phase environment. The vapour delivery system was upgraded from an existing system to include new mass flow controllers, to have greater control of flow through the system, and off the shelf vapour sensors, to collect vapour flow data that could be used for comparison against biosensor activity. The chapter also describes the design and construction of an electronic interface to monitor and control the components of the vapour delivery system, and calibration of the system.

Chapter 9 details the use of the vapour delivery system for testing the functionalised biosensors in the vapour phase. First, the flow behaviour of volatile organic vapours through the system was validated using onboard reference sensors. The response of a pristine carbon nanotube device to two volatile compounds is then compared to the response of carbon nanotube devices functionalised using the second functionalisation approach discussed in the previous chapter.

Chapter 10 summarises the conclusions drawn from this work, and proposes various related studies which can be undertaken to continue the work described in this thesis.

2. Characteristics of Pristine Carbon Nanotube & Graphene Field Effect Transistors

2.1. Introduction

Several different approaches were followed to fabricate carbon nanotube network and graphene field-effect transistors for biosensor use. The three carbon nanotube film types used for devices were the solvent-deposited, surfactant-deposited and steam-assisted surfactant-deposited (steam-deposited) films discussed in ?@sec-fabrication. As minor changes were made to fabrication processes throughout the thesis, the fabrication dates of devices used are stated, alongside a brief description of the process used at the time. This chapter looks to use the characterisation techniques outlined in ?@sec-fabrication to compare and contrast the device channel morphologies and electrical characteristics resulting from the various methods used. The other aim of this chapter is to show the electrical behaviour of the transistors when exposed to vapour in the vapour delivery system discussed in ?@sec-vapour-sensing-biosensors.

Atomic force microscopy and Raman spectroscopy were performed on the carbon nanotube networks to identify the distribution of carbon nanotube diameters and the extent to which defects were present on the carbon nanotube networks. Electrical characterisation was then used to see how the morphology of each film type affected the performance of the completed devices. Both back-gated and liquid-gated transfer characteristics were compared, and figures of merit from the liquid-gated characteristics were examined. Control measurements were also taken to verify the behaviour of the pristine device as a sensor in both liquid-gated and vapour-phase environments. In the liquid-phase, a salt concentration sensing series was performed with a steam-deposited carbon nanotube network device. The device characteristics were taken and device drift was examined and modelled. The sensing series was performed by successively diluting 1× PBS in the polydimethylsiloxane ‘well’ (electrolyte container) while passing a current through the device, and measuring the current response to dilutions. Various filters were applied to the collected data to better understand the signal change. Finally, device responses to ethyl hexanoate and *trans*-2-hexanal in a vapour-phase environment were measured and compared to that of off-the-shelf reference sensors.

2.2. Carbon Nanotube Network Morphology and Composition

2.2.1. Atomic Force Microscopy

Figure 2.1 shows a side-by-side comparison of the surface morphology of carbon nanotube films fabricated using the methods described in ?@sec-dep-carbon-nanotubes. These images were collected using an atomic force microscope and processed in the manner described in ?@sec-afm-characterisation. As discussed in previous works using solvent-based deposition techniques for depositing carbon nanotubes, in each network multi-tube bundles form due to strong mutual attraction between nanotubes [27]–[30]. However, when surfactants are present, they adsorb onto the carbon nanotubes and form a highly repulsive structure able to overcome the strong attraction between nanotubes. This repulsion keeps the individual carbon nanotubes relatively isolated [31]–[36]. The diameter range provided by the supplier for the individual carbon nanotubes used is 1.2 – 1.7 nm, while the length range is 0.3 – 5.0 μm (Nanointegris).

It has previously been demonstrated that the diameter range of deposited single-walled carbon nanotubes can be modelled via a normal or Gaussian distribution [37]–[39]. However, when the height profiles from the $2.5 \mu\text{m} \times 2.5 \mu\text{m}$ AFM images are directly extracted and binned, as shown in Figure 2.1, the histograms obtained do not follow a normal distribution. One reason for this result is that the carbon nanotubes do not lie perfectly flat on the substrate surface, as the SiO_2 substrate and the carbon nanotubes each possess some surface roughness. To find the contribution of substrate surface roughness to the height profile histogram corresponding to each network deposition method, SiO_2 substrates were modified using the same processes as in Figure 2.1 but without carbon nanotubes present in the solutions used. $2.5 \mu\text{m} \times 2.5 \mu\text{m}$ AFM images of the modified surfaces are shown in Figure 2.2.

In Figure 2.2, it appears that each substrate surface has a roughness that follows a normal distribution with some degree of skewness. Figure 2.2 (b) and Figure 2.2 (d) are negatively skewed distributions. The equation for a skew-normal distribution is given in Equation 2.1.

$$f(x) = 2\phi(x)\Phi(\alpha x) \quad (2.1)$$

Within Equation 2.1, α is the ‘slant parameter’ which indicates the skewness of the distribution, $\phi(x)$ is the standard normal distribution and $\Phi(x)$ is the corresponding cumulative distribution function. In the most general case, Equation 2.1 can be modified with the ‘location parameter’ ξ and ‘scale parameter’ ω . These variables respectively correspond to the mean and standard deviation of the skew-free normal distribution when α is set equal to zero. These parameters are inserted into Equation 2.1 by setting $x \rightarrow (x - \xi)/\omega$ and replacing the factor 2 with $2/\omega$ [40]. The fitted skew-normal distribution

2.2. Carbon Nanotube Network Morphology and Composition

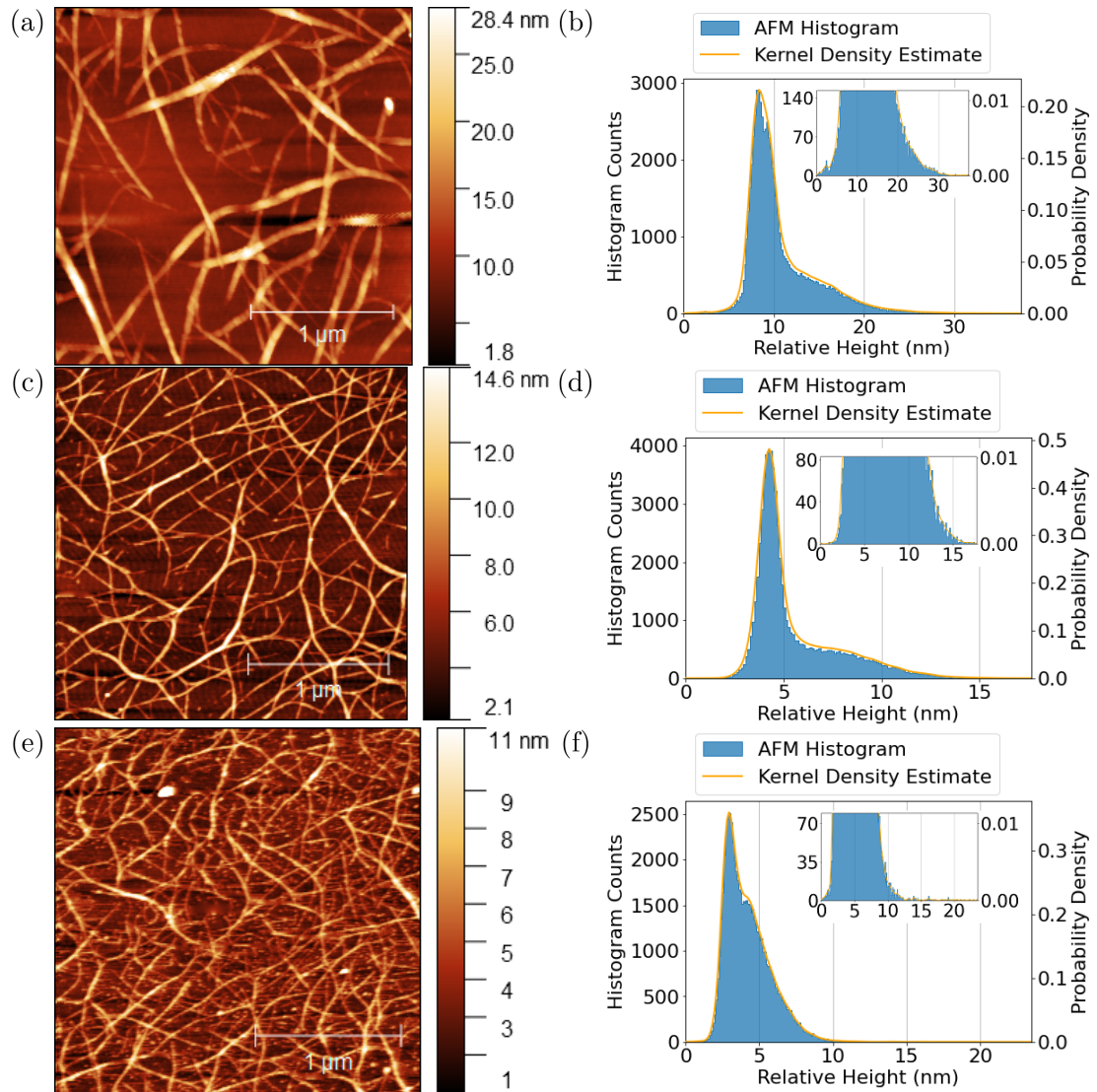


Figure 2.1.: $2.5 \mu\text{m} \times 2.5 \mu\text{m}$ atomic force microscope (AFM) images of carbon nanotube films deposited using various methods, shown side-by-side with histogram height distributions and kernel density estimate (KDE) plots corresponding to each image. The network shown in (a) with height distribution shown in (b) was deposited in solvent, the network shown in (c) with height distribution shown in (d) was dropcast in surfactant, and the network shown in (e) with height distribution shown in (f) was dropcast in surfactant with steam present.

2. Characteristics of Pristine Carbon Nanotube & Graphene Field Effect Transistors

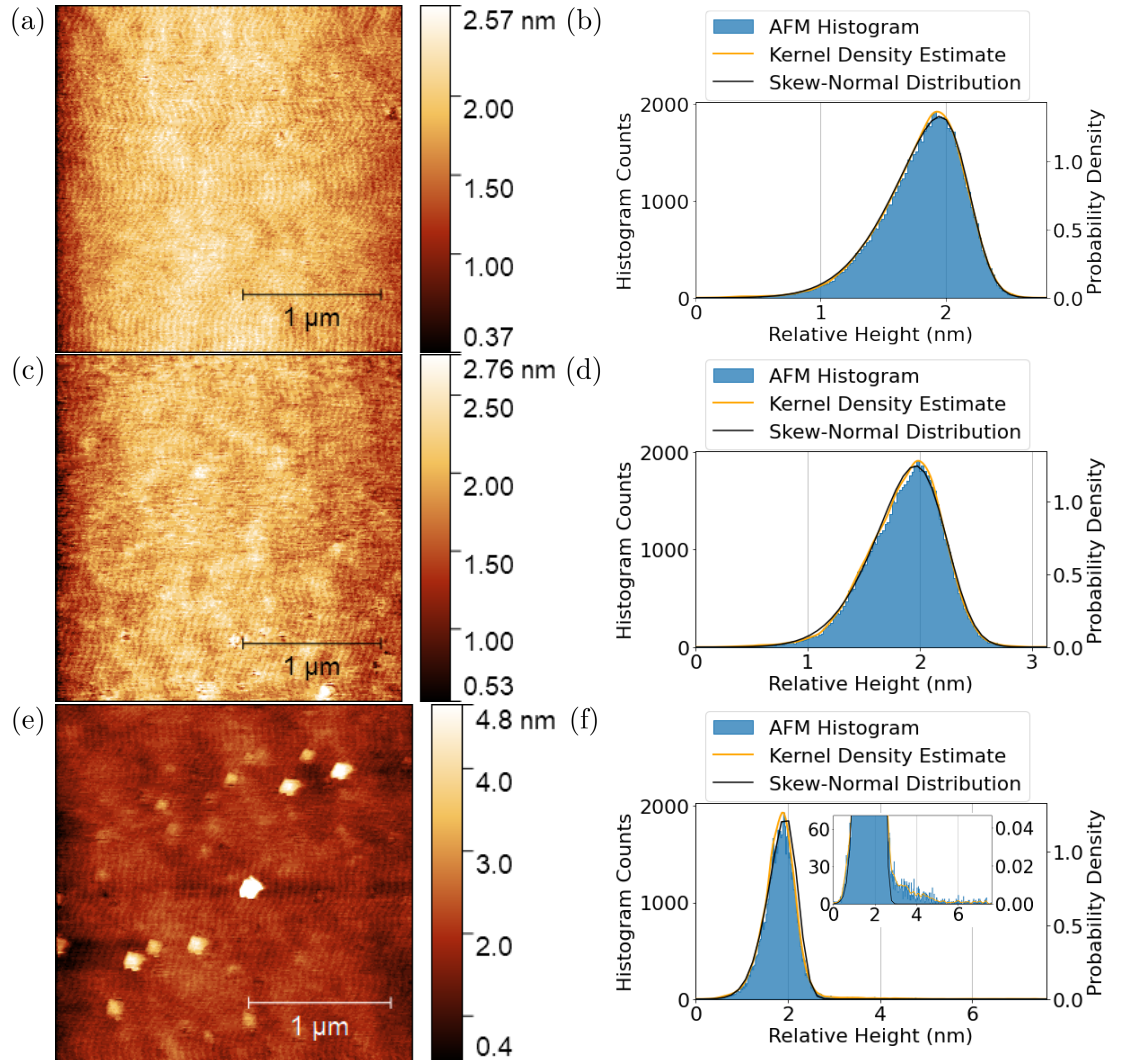


Figure 2.2.: $2.5 \mu\text{m} \times 2.5 \mu\text{m}$ atomic force microscope (AFM) images of SiO_2 substrates alongside histogram height distributions and KDE plots corresponding to each image. The substrate in (a) and (b) was exposed to solvent, the substrate in (c) and (d) was exposed to surfactant, and the substrate in (e) and (f) was exposed to surfactant with steam present. The inset in (f) shows a close-up view of the long tail of the distribution.

2.2. Carbon Nanotube Network Morphology and Composition

in Figure 2.2 (b) has $\alpha = -3.2$, $\xi = 2.2$ nm and $\omega = 0.5$ nm, while in Figure 2.2 (d) $\alpha = -2.2$, $\xi = 2.2$ nm and $\omega = 0.5$ nm. The close correspondence of ξ and ω between these distributions implies that the skewness is a variable imaging or processing artifact rather than a physical property of the surface. Without distortion, the roughness of a clean SiO_2 surface should follow a normal distribution [41].

Figure 2.2 (f) has a pronounced positive skew ~ 5.5 nm in length. The tail results from the droplets observed in Figure 2.2 (e), which may be condensation from the steam or surfactant residue trapped by the steam environment [39], [42]. If the contamination identified here is surfactant, this could have negative effects on both sensitivity of carbon nanotubes and also could damage the attached biological elements. Attempting to fit a skew-normal distribution to this histogram fails when all three variables are allowed to vary, which results from the presence of the tail. Instead, previous values obtained for ξ and ω can be fixed at ξ and ω at 2.2 nm and 0.5 nm respectively in the fitting process, assuming that these values are characteristic of the imaging process used and not the substrate. In this fitting process, therefore, only α was allowed to change. The resulting fitted distribution is shown in Figure 2.2 (f), with $\alpha = -2.4$. The distribution closely fits the negative tail of the histogram, but deviates from the positive tail due to the presence of the droplets. This deviation is small and the fit is otherwise good quality, with an R-squared value of 0.98.

In the atomic force microscope images of the more highly bundled networks, it is easy to distinguish the carbon nanotube bundles from the substrate background by eye. Therefore, it was reasonably straightforward to use techniques similar to those previously outlined by Vobornik *et al.* for network morphology analysis [39]. In the Gwyddion software package, a coloured height threshold or “mask” was defined that minimally covered all regions of exposed substrate. The mask corresponding to each film is shown in Figure 2.3 (a)-(b). The median substrate height within the masked region was 8.9 ± 0.1 nm for the solvent-deposited film, and 4.3 ± 0.1 nm for the surfactant-deposited film. The median height threshold is shown using another mask in Figure 2.3 (c)-(d). These values are dramatically different from the median substrate height of 1.9 ± 0.3 nm obtained from the distributions in Figure 2.2. From comparing the atomic force microscope images in Figure 2.2 with Figure 2.3, it appears unlikely that this difference primarily results from a dramatic increase in substrate surface roughness after carbon nanotube deposition. Instead, it is suggested here that the difference between these values results from the imaging process.

In Figure 2.1, deep streaks or scars with rounded edges can often be found in the close vicinity of larger nanotube bundles and junctions. These features appear to be imaging artifacts, which sometimes sit at heights well below the actual substrate surface. The artifacts result from the microscope tip taking inaccurate surface measurements when moving from scanning a large feature to scanning a much smaller one [43]. Imaging artifacts are highlighted using a mask in Figure 2.3 (e)-(f), with heights of 6.4 ± 0.4 nm and 2.7 ± 0.2 nm for the solvent-deposited and surfactant-deposited films respectively. By adding the median substrate height from Figure 2.2 to the artifact heights, average

2. Characteristics of Pristine Carbon Nanotube & Graphene Field Effect Transistors

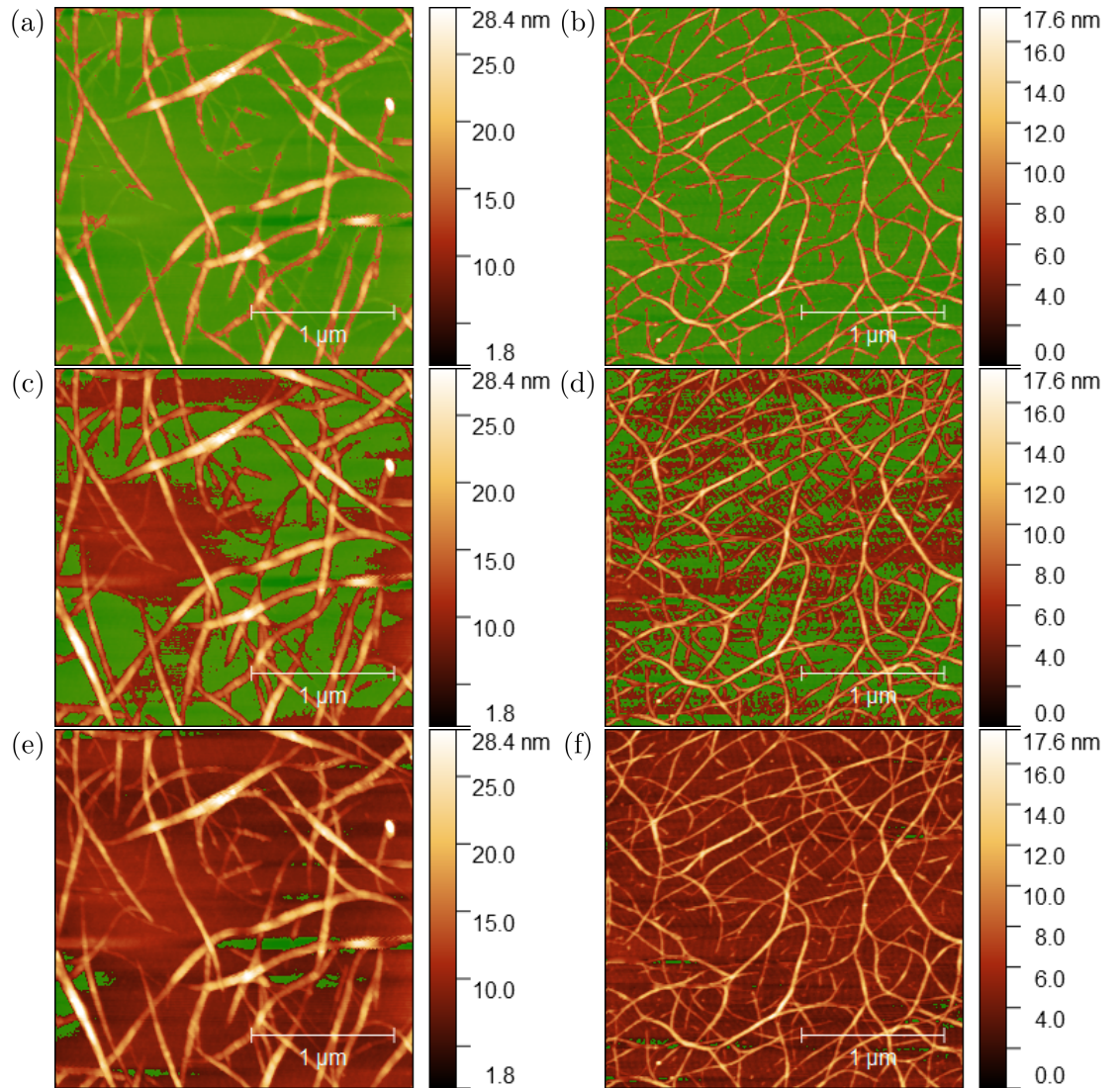


Figure 2.3.: A mask, shaded green, sets a height threshold so that masked features are hidden from the height dataset. The network in (a), (c) and (e) was solvent-deposited, while the network in (b), (d) and (f) was surfactant-deposited. The maximum substrate height of each network is masked in (a) and (b), the median background height is masked in (c) and (d), while outlier artifacts have been masked in (e) and (f).

2.2. Carbon Nanotube Network Morphology and Composition

background values of 8.3 ± 0.7 nm and 4.6 ± 0.5 nm are obtained for each film, both within error of the median substrate heights obtained using Figure 2.3. It can be stated with confidence that the median value obtained from the substrate mask is representative of the actual average substrate level relative to the carbon nanotubes present, unaffected by image artifact outliers. These median values can be used to compare the height of carbon nanotube bundles to the average height of the surrounding substrate, following the same approach as Vobornik *et al.* [39].

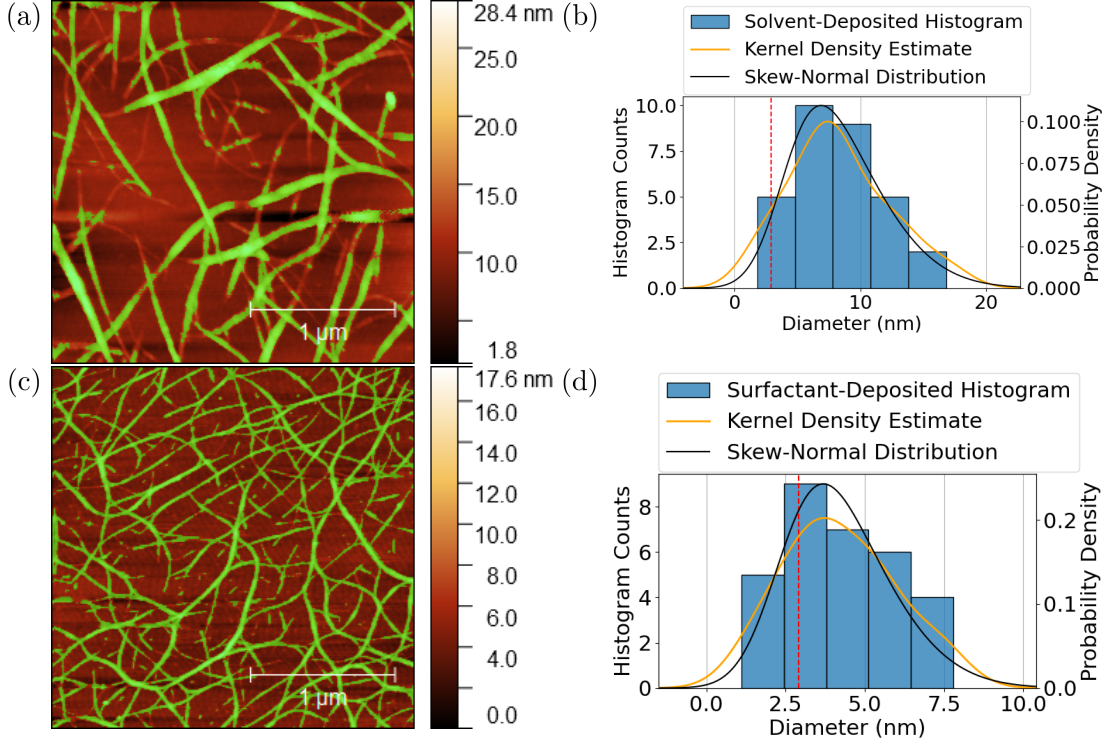


Figure 2.4.: Histogram height distributions for each carbon nanotube network with corresponding kernel density estimate plots collected via the morphology analysis method outlined by Vobornik *et al.* [39]. The histogram for the solvent-deposited network in (a) is shown in (b) and the histogram for the surfactant-deposited network in (c) is shown in (d). The red dotted line represents the lower bound for multi-tube bundles at 2.9 nm, assuming the minimum nanotube diameter is 1.45 nm.

Five successive diameter measurements of 30 carbon nanotube bundles distributed evenly across the network were collected using Gwyddion. Measurements were not taken at bundle junctions. The average of five values for each carbon nanotube bundle was then taken and the corresponding background height of the substrate subtracted. The 30 height values were sorted into five equal-sized bins, as shown in Figure 2.4. Each histogram appears to follow a moderately positive-skewed normal distribution, different to the skew-free normal distribution found in previous works [37]–[39]. The skew is likely

2. Characteristics of Pristine Carbon Nanotube & Graphene Field Effect Transistors

to be another imaging artifact. The force of the atomic force microscope tip is known to cause larger bundles to undergo some degree of compression, and the resulting systematic underestimation of their height may be responsible for the distribution skewness [39]. The fitted skew-normal distribution in Figure 2.4 (b) has $\alpha = 2.5$ (slant, indicates skew), $\xi = 4.0$ nm (location, indicates mean), and $\omega = 5.8$ nm (scale, indicates standard deviation), while the distribution in Figure 2.4 (d) has $\alpha = 2.2$, $\xi = 2.4$ nm, and $\omega = 2.5$ nm. The probability density for the carbon nanotube bundle histogram drops to approximately zero at 0 nm, an indication that each fit is physically realistic.

Table 2.1.: The first eight optimised ratios of 2D packed circle diameter to encompassing circle diameter, given to 3 s.f. (encompassing circle diameter = d , number of packed circles = n , approximate packed circle diameter = d_n).

n	2	3	4	5	6	7	8	9
d/d_n	2.00	2.15	2.41	2.70	3.00	3.00	3.30	3.61

Table 2.2.: The median of histogram distributions for solvent-deposited and surfactant-deposited carbon nanotube films, alongside rough estimates for the number of nanotubes present per median bundle, the estimated proportion of multi-tube bundles present across the network and the proportion of substrate covered by the nanotubes.

	Median Bundle Diameter (nm)	Tubes per Median Bundle	% Multi-Tube Bundles	% Nanotube Coverage
Solvent-deposited	7.8 ± 4.0	21	> 95%	22 – 61%
Surfactant-deposited	3.9 ± 1.8	4	> 78%	27 – 64%

Analysis of carbon nanotube network morphology can be simplified by assuming the component nanotubes are cylinders, follow 2D packing and are of equal diameter [28]. Table 2.1 shows the relationship between the diameter of a bundle of 2D packed cylinders and their constituent diameters. Assuming an average carbon nanotube diameter of 1.45 nm, it is possible to use Table 2.1 to find the approximate number of nanotubes, n , present in the median bundle size of a film [44], [45]. An estimate of the relative proportion of multi-tube bundles in a film can be found by taking the integral of each probability distribution with a lower bound of 2.9 nm, the minimum multi-tube bundle size for 1.45 nm diameter nanotubes. Since the area under the curve represents the probability a bundle will have a particular diameter, the ratio of the bounded integral to the unbounded integral gives a reasonable estimate of the proportion of multi-tube bundles relative to single nanotubes. The proportion of substrate covered by nanotubes

2.2. Carbon Nanotube Network Morphology and Composition

can be determined by comparing the projected surface area of the masks in Figure 2.3 (a)-(d) with the full image area.

These estimates are all shown in Table 2.2, with the caveat that median bundle diameter is likely being underestimated due to tip compression [39]. Alternative estimates for median bundle diameter can be obtained by inverting the mask shown in Figure 2.3 (a)-(b), as shown in Figure 2.4 (a) and (c), and finding the median heights of each masked region, which are 15.9 ± 0.1 nm and 8.2 ± 0.1 nm respectively. By subtracting the median substrate height of each image, 8.9 ± 0.1 nm and 4.3 ± 0.1 nm, alternative median bundle diameters of 7.0 ± 0.2 nm and 3.9 ± 0.2 nm are found, closely in line with the values in Table 2.2. Both the carbon nanotube bundle diameter median and standard deviation are small for surfactant-deposited films when compared to the median and standard deviation of solvent-deposited films. However, despite the presence of surfactant, it is apparent both from Figure 2.4 and Table 2.2 that most surfactant-dispersed carbon nanotubes are not deposited individually. It is possible that the bundling of surfactant-dispersed carbon nanotubes occurs as nanotubes are deposited onto the surface, as this bonding process may disrupt the repulsive forces from the surfactant coating and allow attractive forces to temporarily dominate.

Dense Nanotube Networks

Both the solvent-deposited and surfactant-deposited networks seen in Figure 2.1 (a)-(d) are relatively sparse compared to the steam-deposited film in Figure 2.1 (e)-(f). Because it becomes difficult to distinguish between small nanotubes and the surrounding substrate, it is not immediately clear whether the method of Vobornik *et al.* can be used. The steam-deposited film appears as a dense network of single and less-bundled nanotubes, with larger bundles scattered throughout. A similar masking approach to the one used earlier can be used, where all regions of the image not covered by highly bundled nanotubes are masked, as shown in Figure 2.5 (a). The median height of the masked region is 2.9 ± 0.1 nm, with this height shaded in Figure 2.5 (b). Artifacts of height 0.7 ± 0.2 nm are also present in the top-left corner of the image, as shown in Figure 2.5 (c). Subtracting artifacts from the median height gives 2.2 ± 0.3 nm, which is within the margin of error of the actual median substrate height of 1.9 ± 0.3 nm taken from Figure 2.2.

Taking binned diameter measurements of the larger bundles in the same manner as earlier leads to the figure in Figure 2.5 (d). Unlike the skew-normal distributions seen earlier, the distribution in Figure 2.5 (d) falls to zero at ~ 2 nm. This unphysical result comes from undercounting the large population of smaller nanotubes, which occurs due to the difficulty distinguishing between less-bundled nanotubes and the substrate background. It is still possible to use masking to obtain an estimate of the median bundle height present. The median height of the region not shaded green in Figure 2.5 (a) is 6.0 ± 0.1 nm. The median height of the substrate, 2.9 ± 0.1 nm, can then be subtracted for a median bundle diameter of 3.1 ± 0.2 nm, slightly less than the median bundle diameter

2. Characteristics of Pristine Carbon Nanotube & Graphene Field Effect Transistors

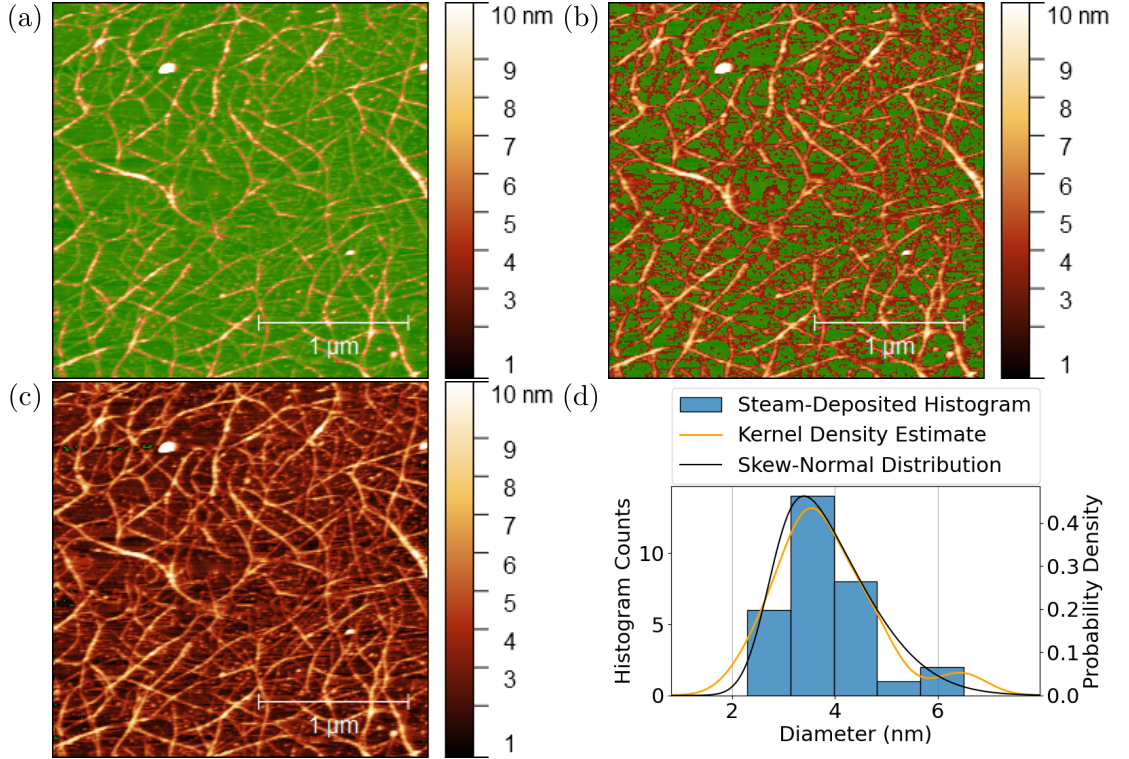


Figure 2.5.: The dense steam-deposited network is covered with a mask showing the maximum height of the substrate and less-bundled carbon nanotubes in (a), a mask showing the median height of this region in (b), and a mask highlighting imaging artifacts in (c). A histogram of bundle measurements above the maximum height of the substrate is shown in (d).

found for the surfactant-deposited film without steam. The surface coverage of the steam-deposited network is also similar to that of the surfactant-deposited network, falling somewhere between 15%, the surface area unmasked in Figure 2.5 (a), and 58%, the surface area unmasked in Figure 2.5 (b).

The discussion in this section gives us a new understanding of the histograms shown in Figure 2.1. It appears that these histograms are linear combinations of skewed normal distributions. These distributions include a negatively-skewed distribution corresponding to the substrate surface and a positively-skewed distribution corresponding to the carbon nanotube bundles. The trough-like image artifacts as well as X and Y junctions between overlapping nanotubes may also form similarly skewed normal distributions as part of the complete image histogram [28]. The linear combination of histograms could be modelled mathematically in order to rapidly extract key parameters from atomic force microscope images [46], but implementing this approach is outside of the scope of this thesis. Introducing steam when depositing with surfactant visibly promotes even surface coverage, but also leads to increased adsorption of water and possibly surfactant

2.2. Carbon Nanotube Network Morphology and Composition

onto the substrate and network. Finding a method of removing the unwanted surfactant or moisture present may be required for robust biosensors [47], [48].

2.2.2. Raman Spectroscopy

Raman spectroscopy was also used to analyse and compare the deposited carbon nanotube networks. Raman spectra were collected from a solvent-deposited carbon nanotube film and a steam-assisted surfactant-deposited film, both on SiO_2 , in the manner described in ?@sec-raman-characterisation. These spectra were then processed using the Python script mentioned in Section B.3. For each location, spectra over two wavenumber ranges were collected. A peak corresponding to the SiO_2 substrate, found in the range between 100 cm^{-1} and 650 cm^{-1} , was used as a reference peak for the normalisation of intensity across the wavenumber range between 1300 cm^{-1} and 1650 cm^{-1} . These normalised spectra are shown in Figure 2.6. In all spectra, a D-band comprising a single D-peak is observed at $\sim 1320 \text{ cm}^{-1}$, and a G-band comprising two G-peaks, G^- and G^+ , is observed between $\sim 1525 \text{ cm}^{-1}$ and $\sim 1650 \text{ cm}^{-1}$. These features are characteristic of networks of metallic and semiconducting carbon nanotubes [49], [50].

Closer inspection of the D-peak and G-peaks in Figure 2.6 can give us important information about network composition. G^- is a minor peak found at $\sim 1570 \text{ cm}^{-1}$, while G^+ is a larger feature at $\sim 1590 \text{ cm}^{-1}$. The G^+ feature describes the in-plane vibration of carbon bonds along the length of the carbon nanotubes and is associated with semiconducting nanotubes, while the G^- feature describes the in-plane vibration of bonds about the nanotube circumference and is associated with metallic nanotubes [50], [51]. The G^+ feature has a sharp Lorentzian lineshape, while the G^- feature has an asymmetric Breit-Wigner-Fano (BWF) lineshape [51], [52]. The splitting between the wavenumber location of the G^- and G^+ local maxima is lower in Figure 2.6 (b) than in Figure 2.6 (a), which may indicate more metallic nanotubes are present in the surfactant-deposited network [51]. The D-peak gives an indication of the defects present in the carbon nanotube atomic structure, which disrupt in-plane lattice vibration [50], [51]. The size of the normalised D-peak appears much lower in Figure 2.6 (a) than in Figure 2.6 (b), indicating the solvent deposition process introduces less defects to the carbon nanotubes than surfactant-mediated deposition.

Carbon nanotube structural disorder can be quantified by comparing the relative magnitude of the D-peak and G^+ -peak intensity [49], [50]. Figure 2.6 (c) compares the ratio between D-peak and G^+ -peak intensity across all nine positions across the solvent-deposited and the surfactant-deposited films. The spread of values for the I_D/I_G ratio is lower for the steam-deposited network. This spatially homogeneous vibrational behaviour reflects the steam-deposited film being more evenly distributed, as discussed in Section 2.2. It is also observed that I_D/I_G is larger for the steam-deposited films than for the solvent-deposited films, indicating more defects are present in the steam-deposited film. These defects may be charge impurities introduced by adsorbed water or surfactant [42]. The size of the G^- feature relative to the G^+ feature can also be used

2. Characteristics of Pristine Carbon Nanotube & Graphene Field Effect Transistors

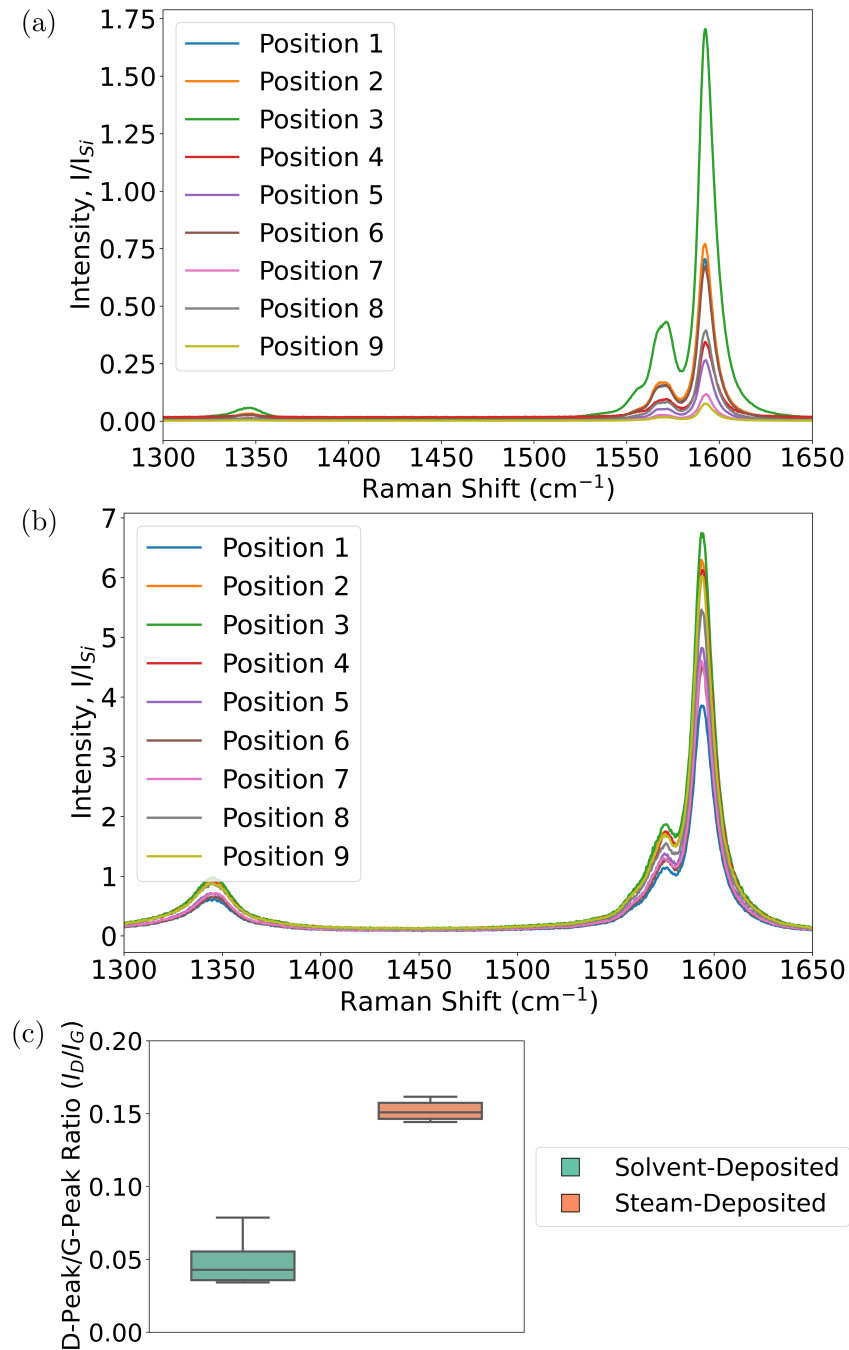


Figure 2.6.: A series of nine Raman spectra at different locations across a $40 \mu\text{m} \times 100 \mu\text{m}$ carbon nanotube film region, where (a) shows spectra from a film deposited using solvent while (b) shows spectra from a film deposited with surfactant in the presence of steam. (c) shows a histogram of the range of D-peak/G⁺-peak spectral ratios corresponding to each film.

to detect charge polarisation due to surfactant presence, though since the G^- feature is also sensitive to bundle size, it cannot be used for a direct comparison of surfactant presence for the films in Figure 2.6. However, if the defects are surfactant, the I_{G^-}/I_{G^+} ratio could be useful for comparing films of similar morphology before and after cleaning steps aimed at removing surfactant, with possible cleaning approaches discussed in ?@sec-future-work-fabrication.

2.3. Electrical Characteristics of Pristine Devices

2.3.1. Python Analysis

Analysis of electrical measurements was performed using the three Python modules described in Section B.4. The device type being analysed, carbon nanotube or graphene, can be set in the config file. The config file can also be used to add annotations to any plot, to set the procedure for normalising a sensing dataset, and the size of the filter window used for the filters described below. In this work, a filter window of 40 datapoints was used.

The first of the three modules is for processing sensing datasets. Types of plots produced include normalised plots, plots with fitted curves, plots with the linear baseline drift removed, plots of signal against analyte addition, ‘despiked’ plots, ‘filtered’ plots and plots with any combination of these modifications. This module uses the `scipy.optimize.curve_fit` function when fitting exponential and linear curves to regions of the sensing data. It then returns .csv spreadsheets containing the results of these analyses, including the standard deviation for all calculated parameters. For a linear fit $c_1 t + c_2$, the initial estimates used for c_1 and c_2 were straightforward: $c_1 = 1$ and $c_2 = 0$. For an exponential fit $I_0 \exp(-t/\tau) + I_C$, rough approximations were used for the initial parameters: I_C was set as the final current measurement of the region of interest, I_0 was set as the initial current measurement minus I_C , and τ was set as the time where measured current drops to $e^{-1}I_0 + I_C$.

‘Despiked’ plots had spurious datapoints removed through the use of an interquartile range rolling filter. Datapoints in each window with a z -score above ± 3 were removed from the plotted/processed data. ‘Filtered’ plots had noise reduced using a moving median filter. The moving median filter is more effective at removing noise than a simple moving average. It also has advantages over other filters, such as the Savitzky-Golay or Butterworth filters, when removing noise from data with sharp edges, which is the case for sensing data. Median filtering can also be used for baseline drift compensation, though this approach was not used in this thesis [53]. A simple difference calculation between the mean of the filtered current before an addition and the mean of the filtered current after the addition was performed at each addition for plots of signal against analyte addition, with examples in Figure 2.7. This process gave reasonably consistent results between the case where baseline drift was removed, as shown in Figure 2.7 (a),

2. Characteristics of Pristine Carbon Nanotube & Graphene Field Effect Transistors

or not, as shown in Figure 2.7 (b). This method of calculating signal is therefore robust even when significant drift is present.

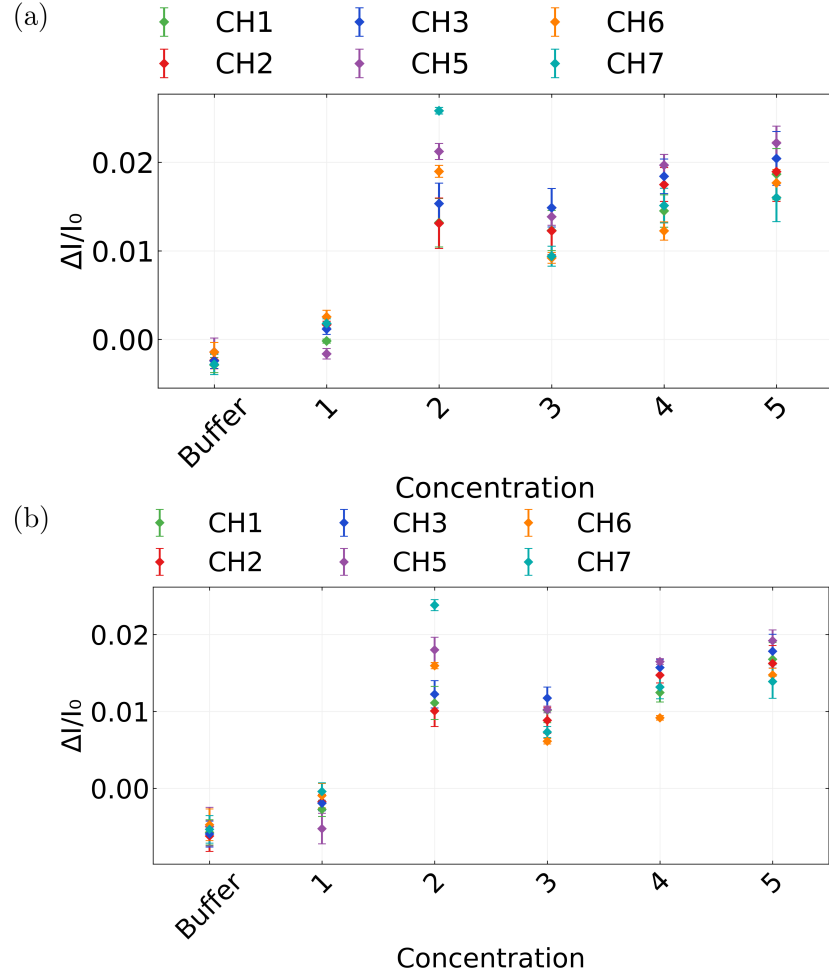


Figure 2.7.: A comparison of signal with analyte addition plots taken from a PBS dilution sensing dataset. In (a), a simple difference before and after addition calculation was performed on filtered data with the baseline drift removed, while in (b), baseline drift was not removed before performing the calculation.

The second module creates combined and individual plots of transfer data collected from eight channels on a single device. In combined plots, shorted or non-conducting channels are removed via setting a maximum and minimum possible on-current in the config file. Various parameters from the transfer characteristics are saved as a spreadsheet along with standard error. These parameters include on current, off current, subthreshold slope and threshold voltage for the carbon nanotube devices, and on current, off current and major Dirac point voltage for graphene devices. The third module allows for comparison

2.3. Electrical Characteristics of Pristine Devices

of transfer measurements taken of the same channel before and after some modification. It also calculates the shift in either threshold voltage or major Dirac voltage of the device.

2.3.2. Graphene Devices

Graphene field-effect transistor devices were electrically characterised in the manner described in [?@sec-electrical-characterisation](#) and analysed using the Python code discussed in Section B.4.

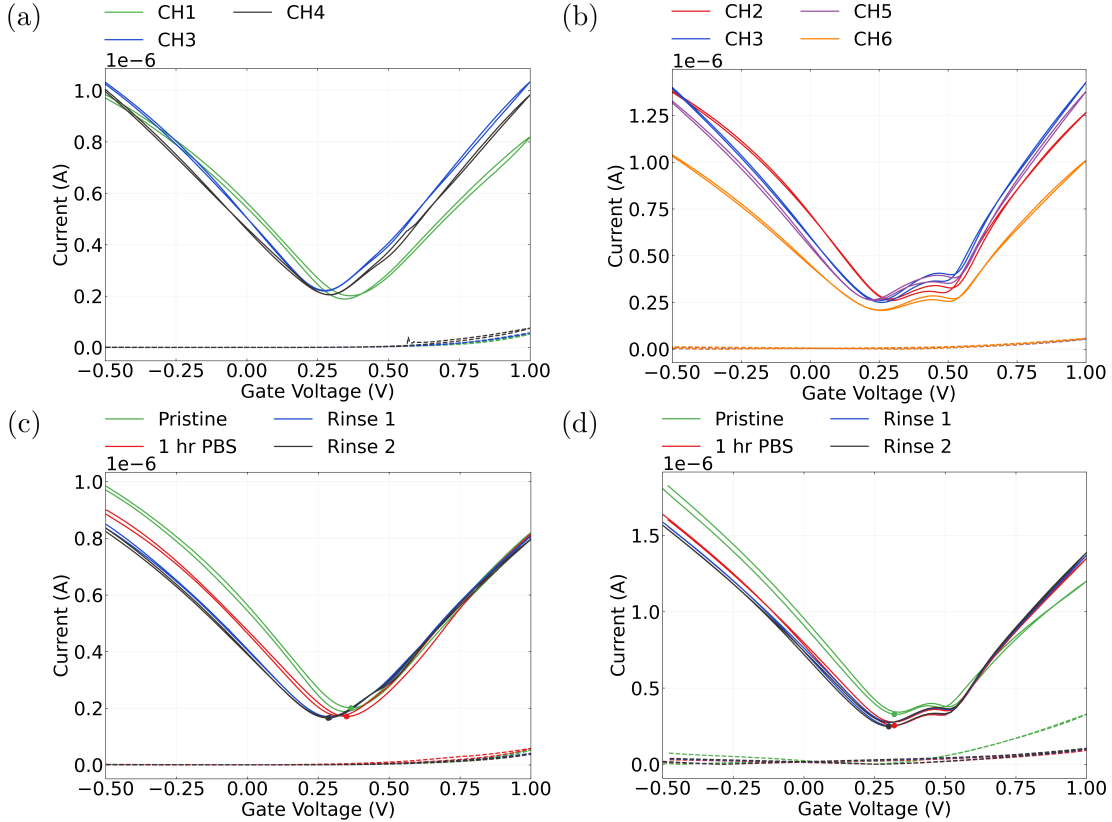


Figure 2.8.: These figures show liquid-gated transfer characteristics of channels from two AZ® 1518 encapsulated graphene devices. The characteristics of working device channels upon initial exposure to 1× PBS are shown in (a) and (b). The transfer characteristics of channel 1 in (a) and channel 5 in (b) after various degrees of exposure to 1× PBS are shown in (c) and (d) respectively, with each transfer sweep numbered in the order the sweeps were taken. The dashed lines correspond to measurements of gate leakage current.

Figure 2.8 (a) and (b) show the liquid-gated transfer characteristics of two graphene devices. These devices were fabricated prior to Jun 2021. Both devices exhibit the

2. Characteristics of Pristine Carbon Nanotube & Graphene Field Effect Transistors

ambipolar characteristics typical of liquid-gated graphene devices [54]–[57]. As with the carbon nanotube network devices, leakage current remained below $\sim 1 \times 10^{-7}$ V across both the forward and reverse sweep. Hysteresis between the forward and reverse sweep is caused by trapping of charge within and on the surface of the SiO_2 dielectric [58]. In this work, the global minimum of the transfer characteristic is referred to as the ‘major’ Dirac point while the second Dirac point is referred to as the ‘minor’ Dirac point. The major Dirac point for these devices is slightly to the right of $V = 0$ V, which indicates *p*-doping of the channel. This slight *p*-doping is a result of adsorption of oxygen and water from the air or from residual photoresist [57], [59], [60]. Some devices exhibited double Dirac point behaviour, as seen in Figure 2.8 (b).

Figure 2.8 (c) and (d) show the effect of $1\times$ PBS on the graphene channels. The channels were measured on exposure to $1\times$ PBS, after exposure to $1\times$ PBS for one hour, and after two successive rinse steps. A slight negative shift of the major Dirac point was observed. This effect is possibly a result of gate bias stress, where successive transfer sweeps introduce charge traps to the graphene layer and alter the current level at a given gate voltage [61], [62]. This effect may also be due to the removal of *p*-doped contamination after rinsing, such as adsorbed oxygen or resist residue, causing interfacial charge traps to empty and resulting in a negative shift of the major Dirac point [57], [58], [63]. Table 2.3 shows the on-off ratio and major Dirac point voltage of the graphene devices after each modification. Apart from the previously-mentioned slight negative shift of the major Dirac point, these values were highly consistent before and after exposure to $1\times$ PBS.

Table 2.3.: Average on-off ratio and major Dirac point voltage for AZ® 1518 encapsulated liquid-gated graphene transistor channels at various stages of exposure to $1\times$ PBS. Electrical characteristics were taken of 6 channels total, three channels from each of two devices.

	1X PBS: Initial	1X PBS: After 1 hr	1X PBS: Rinse
On-Off Ratio (arb.)	5.1 ± 0.3	5.0 ± 0.7	5.0 ± 0.6
Dirac Point Voltage (V)	0.28 ± 0.04	0.31 ± 0.03	0.28 ± 0.02

2.3.3. Carbon Nanotube Network Devices

Each carbon nanotube device fabricated was electrically characterised as described in ?@sec-electrical-characterisation, and electrical data was analysed using the Python code discussed in Section B.4. Devices with a 100 nm or 300 nm SiO_2 layer were used for liquid gated measurements, and devices with a 100 nm SiO_2 layer were used for back-gated measurements. Figure 2.9 displays multi-channel measurements of representative devices fabricated as described in ?@sec-fabrication. To ensure a consistent comparison, all device measurements shown here are from devices fabricated and encapsulated

2.3. Electrical Characteristics of Pristine Devices

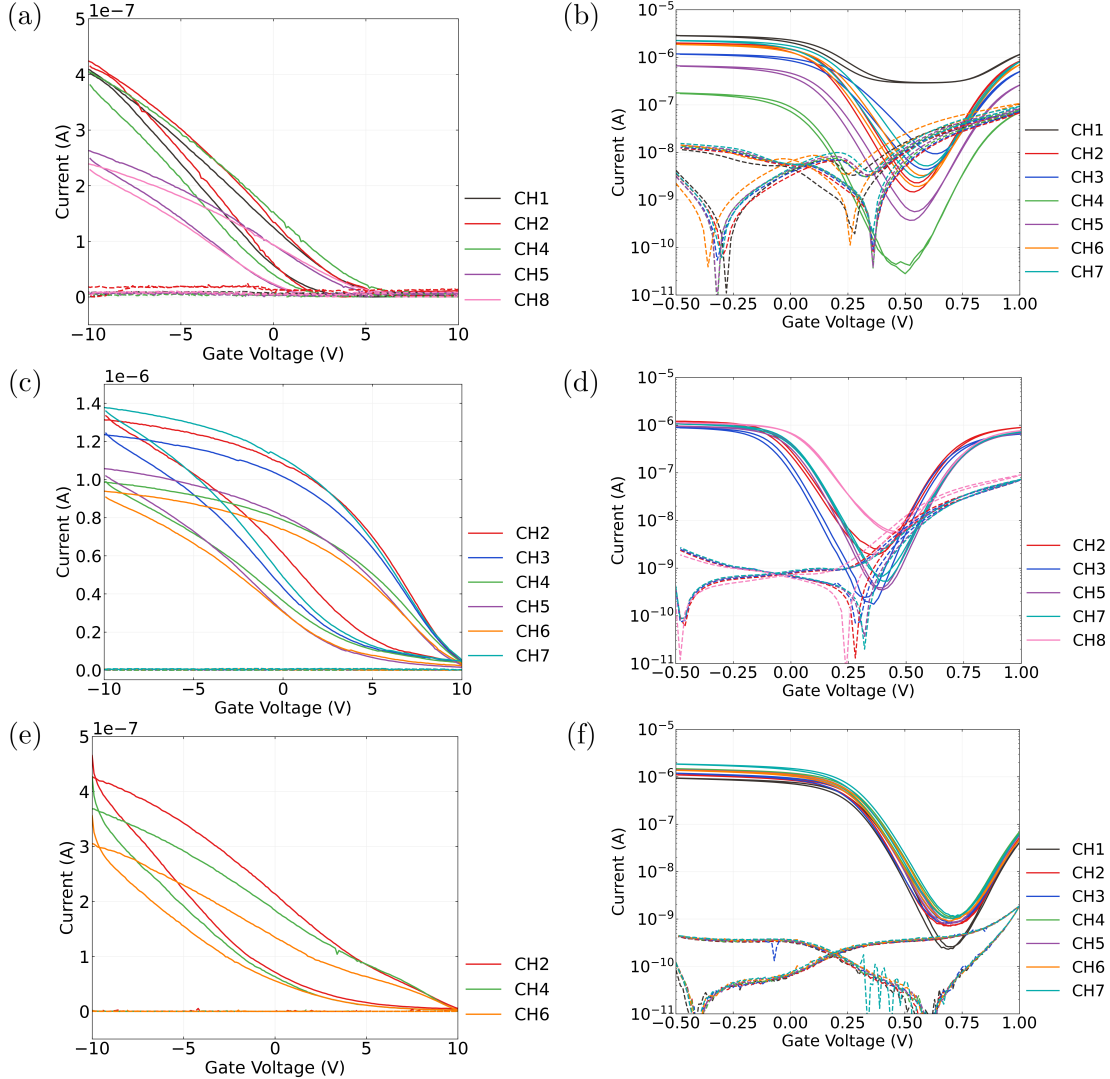


Figure 2.9.: Back-gated (left) and liquid-gated (right) transfer characteristics of AZ[®] 1518 encapsulated field-effect transistors, where the film was deposited with solvent in (a) and (b), deposited with surfactant in (c) and (d), and deposited with surfactant in the presence of steam in (e) and (f). A step size of 100 mV was used for the backgated sweeps in (a), (c) and (e), while a step size of 20 mV was used for the liquid-gated sweeps in (b), (d) and (f). Gate current (leakage current) is shown with a dashed line. The source-drain voltage used for all sweeps was $V_{ds} = 100\text{mV}$, and 1× PBS was used as the buffer for the liquid-gated measurements here.

2. Characteristics of Pristine Carbon Nanotube & Graphene Field Effect Transistors

using only AZ® 1518 photoresist. The channels which did not exhibit reliable transistor characteristics are not shown. These ‘non-working’ channels were either shorted, due to metal remaining on the channel after lift-off, or were very low current, due to a very sparse carbon nanotube network. Devices shown here with a solvent-deposited carbon nanotube network were fabricated prior to Jan 2022; devices with a surfactant-deposited network without steam present were fabricated prior to Jun 2021; devices with a surfactant-deposited network without steam were fabricated prior to Sep 2022.

When characterising devices using the vapour delivery system chip carrier, the setup arrangement meant all measurements were taken using a backgate. Figure 2.9 (a), Figure 2.9 (c) and Figure 2.9 (e) show that backgated devices exhibit *p*-type transistor behaviour. Gate current leakage was negligible, as shown by the dashed line staying close to zero across the sweep. The hysteresis observed was much greater than for the corresponding liquid-gated sweeps on the left. This hysteresis can be explained by the presence of defects or charge traps within and on the surface of the gate-insulating SiO₂ and at interfaces between SiO₂ and carbon nanotubes. The occupancy of these charge traps evolves over time with applied gate voltage [64]–[66]. The devices fabricated with a solvent-based deposition had a significantly lower off-current than the surfactant-deposited devices, which may result from very few metallic nanotubes being present in the less-dense network [67] used to create the device with characteristics shown in Figure 2.9 (a).

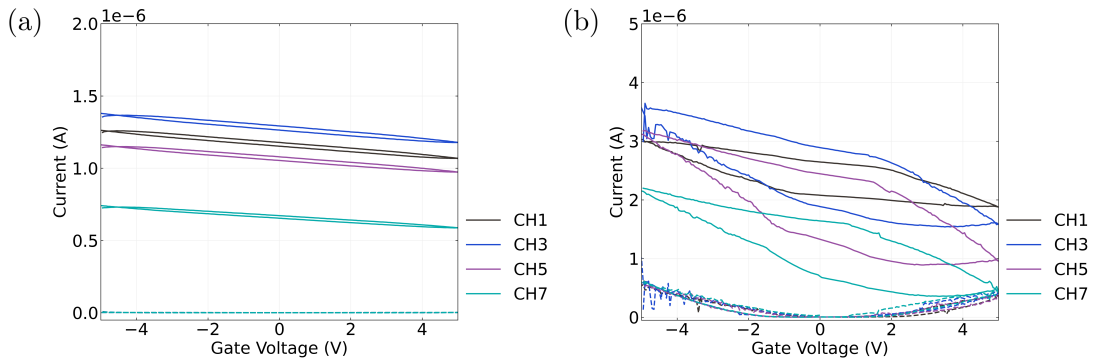


Figure 2.10.: Backgated transfer sweeps were taken of an single unencapsulated device with a 300 nm SiO₂ layer and steam assisted surfactant-deposited carbon nanotube network channels before and after being covered in 50 μ L 1× PBS.

Transfer measurements were taken to determine whether backgated measurements could be taken of an unencapsulated device in the vapour sensor chamber with 1× PBS covering the channels. The use of a backgated configuration with channels in a liquid environment is generally considered less than ideal, since the sensitivity of the device is greatly reduced [68]. Figure 2.10 (a) and (b) respectively show the behaviour of an unencapsulated backgated device before and after being covered by 50 μ L of 1× PBS. The on-off ratio and hysteresis of the channels both increase significantly. The presence of

2.3. Electrical Characteristics of Pristine Devices

water increases hysteresis through introducing charge traps at the SiO_2 surface around the carbon nanotubes and at the surface of the nanotubes themselves [64], [66], [69], [70]. There is also a significant increase in current leakage to the backgate for larger applied voltages, despite the PBS having no visible physical contact with the Si backgate or Cu plane. This leakage current may simply be due to an increase in relative humidity around the device [71].

The liquid-gated devices in Figure 2.9 (b), Figure 2.9 (d) and Figure 2.9 (f) each exhibited ambipolar characteristics, commonly observed in liquid-gated carbon nanotube network FETs [5], [28], [72]–[75]. When devices were appropriately configured, leakage current (shown by the dashed traces) did not exceed $\sim 1 \times 10^{-7}$ V across the forward and reverse sweeps. The devices shown which used steam-deposited carbon nanotube films consistently showed the least hysteresis. Section 2.2.1 demonstrates that the mean diameter of the bundles in these films is ~ 5 nm less than those in films deposited in solvent. Hysteresis is known to scale roughly linearly with bundle diameter, due to trapped charge increasing as bundle density of states is increased [76]. Steam-deposited devices also showed significantly less channel-to-channel variation in electrical characteristics more generally. Channel 1 in Figure 2.9 (b) has a much higher off-current than the other channels of the same device, which appears to be due to a unusually high proportion of metallic carbon nanotubes present in the network conduction pathways of this channel [67], [77].

A summary of key parameters of pristine liquid-gated devices is shown in Figure 2.11. The full dataset consists of three sets of 21 liquid-gated transfer characteristics of working channels, with each set corresponding to the use of a particular method of carbon nanotube network deposition in the device fabrication. Measurements from at least three devices are included in each set. Each entry in the summary corresponds to the average of the specific parameter in the forward and reverse sweep direction. When steam was used for surfactant deposition of films, the resulting devices showed highly consistent channel-to-channel electrical properties. Since the carbon nanotube films on these devices are relatively dense, as seen in Table 2.2, the network should be well above the percolation threshold. As many carbon nanotube pathways connect across the channel in parallel, small variations in the network morphology have less of an impact on the overall channel behaviour [28]. Figure 2.4 and Table 2.2 indicate that the range of bundle sizes is relatively low in the steam-deposited films used in these devices, meaning the electrical behaviour of dominant conduction pathways is more spatially consistent. The highly consistent and reproducible subthreshold regime behaviour between channels seen for steam-deposited devices is a desirable attribute for reliable real-time multiplexed biosensing [5], [72], [78].

Channels from surfactant-deposited film devices usually showed a larger on-off ratio and subthreshold slope than those from solvent-deposited devices. Increasing the ratio of gate-sensitive semiconducting carbon nanotubes to metallic nanotubes tends to increase the on-off ratio [28], [37], [67], [77]. Increasing network density is expected to increase the proportion of metallic nanotubes present [67], and Section 2.2.2 indicates there are

2. Characteristics of Pristine Carbon Nanotube & Graphene Field Effect Transistors

more metallic nanotubes present in the surfactant-deposited films than in the solvent-deposited films. However, percolating conduction pathways dominate device behaviour, and nanotube pathways across the channel with a lower degree of bundling are less likely to contain metallic tubes [28]. Therefore, the larger on-off ratio for surfactant-deposited film devices is likely a result of their reduced nanotube bundle size and reduced bundle size variation relative to solvent-deposited films, as discussed in Section 2.2. The increased on-off ratio also results in a larger subthreshold slope, due to the lowering of off-current across orders of magnitude. A large on-off ratio and subthreshold slope both indicate reduced device power consumption. The relatively large on-off ratio and subthreshold slope of steam-deposited devices are therefore desirable for improved sensor performance [5], [72], [78].

All channels characterised had a positive threshold voltage (V_t). The threshold voltage was largest and most consistent for steam-assisted surfactant-deposited films. The steam-assisted surfactant-deposited devices had an average threshold voltage of 0.37 V, significantly higher than the to solvent-deposited and surfactant-only network devices, with average threshold voltages of 0.27 V and 0.22 V respectively. This increased threshold voltage corresponds to increased *p*-doping of the network [28], [79], [80]. As seen from Figure 2.2 (e)-(f) and Figure 2.6 (c), the steam deposition process leads to the presence of *p*-dopant contamination due to trapped water vapour or surfactant on the carbon nanotubes. It has been previously established that residual surfactant can also enhance the *p*-doping from adsorbed oxygen and water [42], [47], [81]. The analysis by Kane *et al.* shows that the thermal annealing used in this work is likely inadequate for removing residual surfactant. Thermal oxidation of devices may be required for effective desorption of the persistent surfactant, as discussed in ?@sec-future-work-fabrication. Devices using films made with the other CNT deposition techniques have the advantage of not requiring careful treatment to remove surfactant.

The solvent-deposited devices had a slightly larger transconductance at $V_g = 0$ V, the operating voltage used for sensing. As the carbon nanotube networks of surfactant-deposited devices are typically much denser than solvent-deposited (Table 2.2), they should exhibit increased ballistic transport of charge carriers, increased mobility and therefore increased transconductance [67]. The observation of slightly reduced transconductance in surfactant-deposited devices ($\sim 1 \mu\text{S}$) relative to solvent-deposited devices ($> 2 \mu\text{S}$) in Figure 2.11 (b) is therefore surprising. However, the transconductance behaviour at $V_g = 0$ V corresponding to each device morphology partly depends on the threshold voltage. The threshold voltage determines the relative position of the transfer curve, which therefore affects the voltage corresponding to maximum transconductance. If $V_g = 0$ V is close to the point of maximum transconductance for solvent-deposited devices, slight shifts in threshold voltage may dramatically lower transconductance at $V_g = 0$ V. Surfactant deposited devices deposited without steam had a lower threshold voltage on average than the solvent-deposited devices, while the steam-assisted surfactant-deposited devices had a higher threshold voltage on average. As a larger transconductance is desirable for enhanced sensitivity and low power operation, restoring the threshold voltage by removing surfactant may be important for device optimisation.

2.4. Aqueous Sensing of Phosphate Buffered Saline Concentration

2.4.1. Control Series and Baseline Drift

To verify the sensitivity of the fabricated field-effect transistors and therefore test their suitability for sensing, control measurements replicating a typical sensing experiment were taken before functionalising the channels of a carbon nanotube network device. The first step to verifying device suitability was ensuring the device showed no response to $1\times$ PBS. This sequence is referred to in this thesis as the ‘PBS control series’. The PDMS well contained $80\ \mu\text{L}$ $1\times$ PBS at 0 s. The PBS control series ran over the first 1800 s, with $20\ \mu\text{L}$ $1\times$ PBS additions at 100 s, 200 s and 300 s, and $20\ \mu\text{L}$ subtractions at 400 s, 500 s and 600 s. The device was left untouched over the next 1200 s to allow the current level to settle. The gate voltage was held at $V_g = 0\ \text{V}$.

Figure 2.12 (a) shows the PBS control series corresponding to each device channel alongside gate current. In both series, there is no clear stepwise response to any addition or subtraction of $1\times$ PBS. Gate leakage current remains negligible across the entire control series, with no change in response to $1\times$ PBS additions. The current has a period of short-term decay followed by much longer term baseline drift, similar to observations by Lin *et al.* and more recently Noyce *et al.* for parallel arrangements of single carbon nanotubes in air or vacuum [62], [82]. This effect results from hysteretic changes in the occupancy of charge traps in and around the substrate and carbon nanotubes. The magnitude of baseline drift is lower for our devices than for those characterised by Noyce *et al.*, which may be a result of numerous device and setup differences which affect the presence of charge traps. These differences include the use of liquid-gating instead of back-gating, a network of carbon nanotubes instead of single nanotubes, a different channel length, a 300 nm instead of 90 nm SiO_2 layer, a gate voltage of 0.0 V instead of -15.0 V, and an asymmetric, liquid-gated transfer sweep over a shorter voltage range when characterising devices before each control series [62].

As a first-order approximation to the longer time constant exponentials discussed by Noyce *et al.* [62], linear fits were performed on each PBS control series from 1200 – 1800 s. These fits are tangent to the curve of the sum of the larger time constant exponentials, and are a close approximation to this curve when higher order terms in the series expansion are approximately zero. This is only the case when $t \ll \tau_i$, where the time interval of interest t is much shorter than the time constants of the larger time constant exponentials, τ_i . These linear fits are shown by the dashed yellow lines in Figure 2.12 (a). The parameters from each fit in Figure 2.12 (a) are shown in Table 2.4, where $I = c_1 t + c_2$. Intriguingly, the fits for channels 1, 5 and 7 are all in parallel within error. Furthermore, the gradient value for each fit in Figure 2.12 (a) is consistent within a 2.6 pA/s range across all channels. The current data from channel 1 is closely approximated by the linear trendline across the entire control series. No short-term decay is present for this channel, indicating the channel has low net trapped charge. It

2. Characteristics of Pristine Carbon Nanotube & Graphene Field Effect Transistors

is unclear why trapped charge is significantly lower for channel 1 than across the rest of the device.

Table 2.4.: The coefficients of linear fits to the PBS control series of each channel between 1200 – 1800 s, where c_1 is the gradient and c_2 is the constant term.

Channels	CH1	CH2	CH3	CH5	CH6	CH7
c_1 (pA/s)	-5.1±0.2	-7.2±0.1	-6.5±0.1	-5.0±0.1	-7.6±0.1	-5.1±0.2
c_2 (μ A)	0.316	0.316	0.308	0.218	0.364	0.332

The long-term linear fits were next subtracted from the raw control series data. Figure 2.12 (b) shows exponential fits to the remaining curve from 0 – 1800 s, which was successful for all channels except channels 1 and 5. The parameters from each fit are shown in Table 2.5, where $I = I_0 \exp(-t/\tau)$. Any constant term I_C resulting from the fit was negligible and so could be neglected. The exponential fits had characteristic time constants τ ranging between 280 – 610 s. Note that the value of peak-to-peak noise is above 5% of the initial current value for all channels. This result indicates that 3 time constants is a sufficient length of time for this short-term baseline drift to decay almost completely for each channels. At most, 1830 ± 150 s is required to minimise the drift present when sensing is performed, which is fulfilled by the chosen length of the control series.

Table 2.5.: The coefficients of exponential fits to the PBS control series of each channel between 0 – 1200 s, after the linear fit has been subtracted, where I_0 is the gradient and τ is the time constant.

Channels	CH2	CH3	CH6	CH7
I_0 (nA)	6.07 ± 0.08	7.19 ± 0.11	5.75 ± 0.12	9.68 ± 0.41
τ (s)	450 ± 10	610 ± 30	280 ± 10	350 ± 30

From this analysis it appears that the baseline drift for the liquid-gated carbon nanotube devices can generally be approximated as a combination of a linear and exponential term. The exponential term corresponds to short-term, fast decaying baseline drift, while the linear term is an approximation to longer-term, slow decaying exponential baseline drift. The lack of response at all of the six PBS addition and removal times gives us confidence that this is a stable baseline which can be used for reliable sensing. Furthermore, the baseline drift can reasonably be approximated as linear after ~ 1800 s. This linear drift has a small gradient of less than -10 pA/s. The relatively small size of this drift makes it easier to distinguish responses due to analyte addition from baseline drift. It can

2.4. Aqueous Sensing of Phosphate Buffered Saline Concentration

therefore be concluded that the 1800 s length of the PBS control series is appropriate for further experimental work.

2.4.2. Sensing Series

A salt concentration sensing series was performed from 1800 s onwards, directly after the PBS control series. The responses to successive dilutions of the PBS gate were recorded to confirm the fabricated devices were sensitive to small environmental changes in their pristine state, to check for spurious signals, and to ensure gate current leakage or other confounding factors were not contributing to sensing responses. The PDMS well contained 80 μL 1 \times PBS at 1800 s. During the series, successive additions of deionised water were made to reduce the concentration of PBS in the well. An initial 1 \times PBS addition was performed at 2100s, to confirm no changes occurred during the PBS control series that would interfere with sensing. All additions to the well in the sensing series and resulting changes to the PBS concentration in the well are shown in Table 2.6.

Table 2.6.: This table shows the times at which 20 μL additions were made to the PDMS well, with 300 s between each addition. The concentration in the well after each addition and the change in concentration after each addition are also shown. The well contained 80 μL of 1 \times PBS at 1800 s. The major component in PBS is NaCl, which has a concentration of 137 mM in 1 \times .

Addition #	1X PBS		DI Water Additions			
	1	2	3	4	5	6
Time (s)	2100	2400	2700	3000	3300	3600
Final PBS volume (μL)	100	120	140	160	180	200
Final PBS concentration	1X	0.83X	0.71X	0.63X	0.56X	0.50X
Δ PBS concentration	0	-0.17X	-0.12X	-0.09X	-0.07X	-0.06X

Figure 2.13 (a) shows a multiplexed salt concentration sensing series from the channels of a single AZ® 1518 encapsulated device, measured with the NI-PXIe. The gate voltage used was 0 V, which meant current measurements were well above the magnitude of the subthreshold device current. Gate current measurements did not exceed 10 nA at any point. At each of the deionised water addition times, the current traces for at least two out of six channels showed a sharp, transient increase in current followed by a return to an increased baseline. It is well established that changing the salt concentration of the liquid gate has an electrostatic gating effect on the carbon nanotubes or graphene, and changes the transfer characteristics of the channel. This shift in transfer characteristic leads to a real-time signal response to each addition [55], [57], [72].

Using the data in Table 2.4, the linear term approximating baseline drift ($c_1 t$) for each channel can be subtracted from the data in Figure 2.13 (a) to account for the downward

2. Characteristics of Pristine Carbon Nanotube & Graphene Field Effect Transistors

drift. The mean current level just before 1800 s then becomes roughly constant. Next, each channel is normalised relative to their initial mean current level I_0 . Artifacts resulting from PXIE-2737 module lag, single datapoints which fall well below the current level of the immediately preceding and succeeding datapoints, are also removed. This ‘despike’ process uses an interquartile range filter, which is described in Section 2.3.1. The resulting dataset is shown in Figure 2.13 (b). This figure shows that the signal-to-noise ratio remains roughly similar across all channels of the device. However, the behaviour of the initial transient increase with each addition is highly variable across channels and between additions for a single channel.

As measurement of the highly variable initial transient is not useful for robust sensing purposes, a moving median filter was applied, with the implementation of this filter discussed in Section 2.3.1. The filtered data is shown in Figure 2.13 (c). Noise and initial transients are removed completely, while the clearly defined step to a new current baseline is retained. Using the realtime data in Figure 2.13 (c), a plot of signal against addition can be created using the method described in Section 2.3.1, shown in Figure 2.14 (a). This approach illustrates the increase at each step relative to I_0 .

Intriguingly, even though the largest change in PBS concentration occurred at the first deionised water addition (see Table 2.6), there was very little signal change across all channels, while a relatively large change occurred at the second addition. The logarithm of final salt concentration has previously been shown to be proportional to conductance change in the linear on-regime [55]. Figure 2.14 (b) shows the signal change presented in terms of this logarithmic relationship. The median values of the first two additions do not line up well with the overall logarithmic trend; insufficient mixing in the tightly enclosed PDMS well environment for the first few additions may be responsible for this result. Subsequent additions may improve mixing in the well, leading to the change in concentration at the surface of the channel being more representative of the overall concentration in the well.

In Figure 2.13 (b) and Figure 2.13 (c), from around the second deionised water addition onwards, the drift behaviours of individual channels begin to significantly diverge. This deviation from the baseline drift subtracted from the raw data occurs either because the linear fit is only a first-order approximation which weakens with time, or because the additions themselves affect the drift behaviour. Displaying the data as discrete signal changes, as in Figure 2.14 (a), is one way of excluding these deviations (see Section 2.3.1). An alternative way of presenting the signal changes, by normalising relative to both I_0 and the final current reading with the formula $\$(I - I_{\{0\}})/(I_{\{f\}} - I_{\{0\}})\$$, is shown in Figure 2.15. This approach is useful for filtering out remaining unaccounted-for drift behaviour in order to compare the short-term transient responses to additions across the device channels. Furthermore, it lets us better understand how the short-term transient responses affect the longer-term step responses discussed earlier.

Figure 2.15 (a) and Figure 2.15 (c) show that the transient responses to DI water additions vary significantly across the surface of the device. For example, Figure 2.15 (c) shows that in response to the second DI water addition, channel 7 gives a large initial

transient response about twice the size of the step increase between 2600 and 2800 s. Meanwhile, channels 1 and 2 show no transient response above the step increase. Figure 2.15 (c) indicates transient size is based on location across the device, with neighbouring channels showing the most similar behaviour. This spatially-dependent behaviour may indicate transient responses are determined by the location of the channel relative to either the location of water additions or the slightly-variable location of the liquid gate. Larger and longer-lasting transient responses are not entirely removed by the moving median filter, as shown by comparing Figure 2.15 (a) to Figure 2.13 (c), and so careful placement of additions is important when sensing to minimise this effect. However, even the longest-lasting transients appear to decay to zero within about 200 s, demonstrating that a 200 s spacing between additions at minimum is necessary for reliable real-time liquid-gated sensing using this setup.

To explore the effect of gate voltage on signal-to-noise ratio in the subthreshold regime, two PBS control and salt concentration sensing series were performed with the same channel at different gate voltages, shown in Figure 2.16 (a) with coloured dashed lines. Figure 2.16 (b) shows the initial PBS and DI water additions made after 1800 s. Previous work on the signal-to-noise ratio for liquid-gated, encapsulated carbon nanotube devices suggests that gating devices close to V_{gap} should give a larger signal-to-noise ratio for salt concentration changes [72]. However, in this case, improved signal-to-noise ratio was observed when gated at a voltage further removed from V_{gap} . This discrepancy could be a result of the use of a network of carbon nanotubes rather than a single nanotube, where gating may have less of an impact on noise. Alternatively, it could be a result of a lack of mixing in the well setup used, leading to inconsistent signal sizes with concentration change. Heller *et al.* used a flow cell during their signal-to-ratio work [72]. By using a flow cell with our devices, it would be possible to understand the role of mixing in the salt concentration work shown in this section.

2.5. Conclusion

To ensure fabricated transistors were suitable for biosensing purposes, the morphology and electrical properties of the pristine carbon nanotube and graphene transistors were investigated.

The morphology of the carbon nanotube networks was found to have a significant impact on the electrical characteristics of the devices, determined by comparison of the skew-normal height profile of the carbon nanotube network and the key electrical parameters of a selection of carbon nanotube devices. When carbon nanotubes were deposited in solvent, the resulting networks were highly bundled (> 95 % bundled) and there were large variations in bundle diameter. Liquid-gated devices created using these carbon nanotube films had highly variable on-off ratios due to the large variation in the conductive pathways available. In contrast, devices using films fabricated using surfactant with steam present showed lower bundling and less variation in bundle diameter. These

2. Characteristics of Pristine Carbon Nanotube & Graphene Field Effect Transistors

films were used to create devices with improved device-to-device reproducibility of device characteristics, particularly on-off ratio. These devices also exhibited lower hysteresis, due to the relatively consistent bundle diameters and high density of these networks. When performing multiplexed sensing, consistent channel behaviour is highly desirable since comparing sensing behaviour between channels is more straightforward.

However, less bundled networks had the most surface contamination present. Atomic force microscopy indicated the presence of contamination due to steam-assisted deposition. Raman spectroscopy showed that steam deposition led to increased defects in the network, with a significantly increased D -peak to G^+ -peak height ratio. The average threshold voltage for steam-assisted surfactant-deposited network devices was significantly higher than the average threshold voltage for solvent-deposited devices, indicating these defects *p*-dope the network. The shift in threshold voltage was found to reduce device transconductance, a parameter which should be maximised for optimal sensing. Furthermore, the presence of surfactant or even trapped water could potentially have negative impacts on device functionalisation, discussed further in **?@sec-noncovalent-functionalisation**. Techniques to remove contaminants may need to be explored in more detail in future works. Thermal oxidation of carbon nanotube films could be used to resolve this issue, and this is discussed further in **?@sec-future-work-fabrication**.

Constant voltage real-time measurements of the carbon nanotube field-effect transistor devices had a characteristic drift that could be modelled using both a linear and exponential term. This was true for both liquid-gated and back-gated devices. The linear term of liquid-gated baseline drift had a reasonably consistent gradient between device channels, indicating that similar drift behaviour should be reproducible between devices fabricated in the same manner. The exponential behaviour was less consistent, indicating that this hysteresis behaviour is less closely correlated with the fabrication process. A control series length of 1800 s was used, as this period was sufficient to minimise exponential drift during sensing for all the channels tested. The linear and exponential terms for back-gated baseline drift under nitrogen flow were significantly higher than all measurements for liquid-gated drift. A longer control series length of 2400 s was therefore used to minimise exponential drift when vapour sensing.

A PBS dilution sensing series was used to verify that the carbon nanotube transistor devices were highly sensitive to changes in an aqueous environment. The expected logarithmic signal response behaviour was observed when detecting dilutions of PBS in a liquid-gate environment. Signal size relative to baseline drift was highly consistent between channels, which is promising for multiplexing work. Deviations from the logarithmic trend possibly indicated insufficient mixing within the PDMS well during sensing, which may be addressed in future aqueous sensing work by using a flow cell. This experiment is a useful control for sensing using functionalised devices. It is important to confirm that the devices are highly sensitive, while also being able to discern whether a signal response is due to interaction with an attached biomolecule or whether the carbon nanotubes themselves are responding.

2.5. Conclusion

Graphene field-effect transistor devices were often found to possess a double-minima feature, which appears to be the result of a lack of doping from the metal contacts in the center of the device channels. These double Dirac points are unlikely to have any significant effect on the sensing behaviour of graphene devices. The graphene device characteristics were found to be highly consistent after 1 hour exposure to PBS with minimal drift. There was some indications from the transfer characteristics that *p*-dopants were present on the graphene surface. Salt concentration and vapour sensing with graphene FETs are not shown in this thesis, but it is important to perform similar device verification and control testing when using a batch of graphene devices for biofunctionalised sensing.

2. Characteristics of Pristine Carbon Nanotube & Graphene Field Effect Transistors

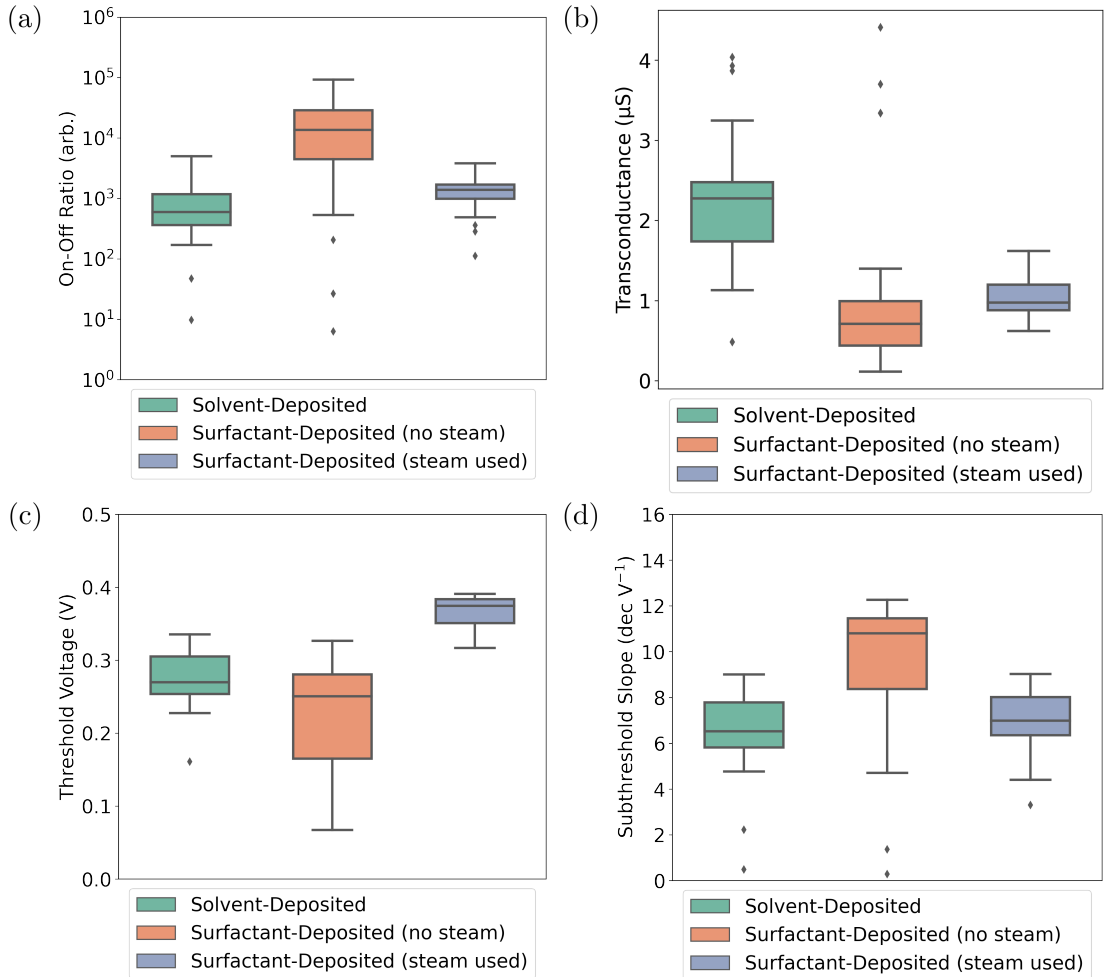


Figure 2.11.: These boxplots illustrate the statistical distribution of (a) the on-off ratio, (b) the transconductance at $V_g = 0$ V, (c) the threshold voltage and (d) the subthreshold slope of liquid-gated and AZ® 1518 encapsulated transistor channels fabricated using solvent-deposited, surfactant-deposited or steam-assisted surfactant-deposited methods. For each deposition type, electrical characteristics were taken of 21 channels of at least three separate devices. The boxes indicate the 25th and 75th percentile of the distribution.

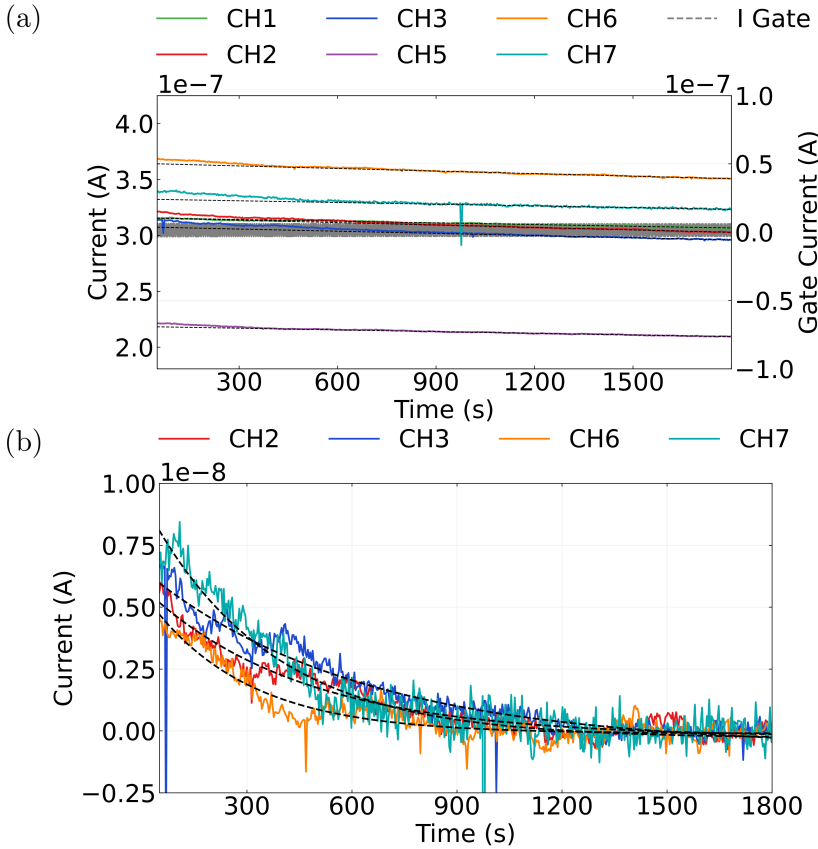


Figure 2.12.: The transfer characteristics in (a) were taken of the steam-deposited carbon nanotube field-effect transistor used here for an example of salt concentration sensing. The absolute values of measurements are shown, so that negative values resulting from measurement error can be visualised. Linear fits to the PBS control series from each channel from 1200 s onwards are shown in (b), while exponential fits to the PBS control series from 0 – 1200 s with the linear fit subtracted are shown in (c). No significant response to PBS additions are seen at any of the addition times from 100 – 600 s.

2. Characteristics of Pristine Carbon Nanotube & Graphene Field Effect Transistors

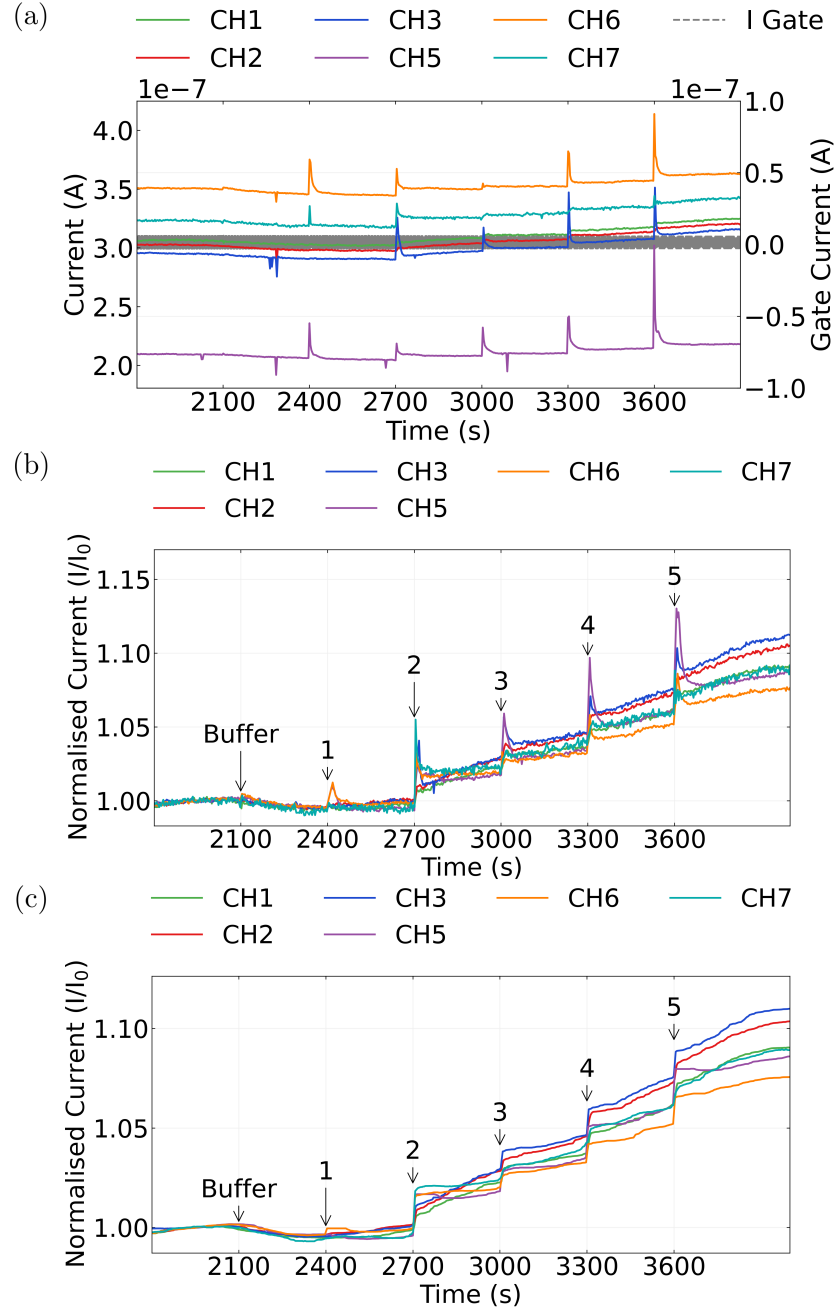


Figure 2.13.: A multiplexed salt concentration sensing series across eight channels of a steam-assisted surfactant-deposited carbon nanotube device. The source-drain voltage V_{ds} was 100 mV, and gate voltage V_g was 0 V. In (a), the raw current measurements for each channel are shown alongside gate current. The same measurements after despiking, removal of baseline drift and normalisation to initial current are shown in (b), (c) shows the data in (b) after being processed with a moving median filter.

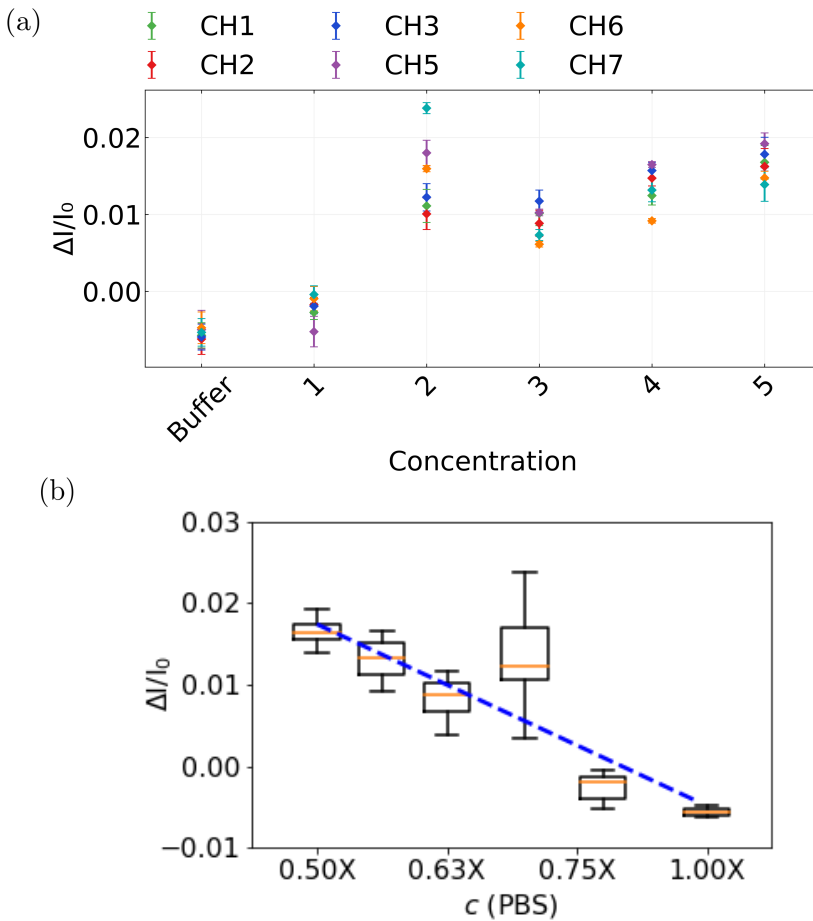


Figure 2.14.: The signal changes in Figure 2.13 (c) are shown in (a). This signal data is then shown in box plot format in (b) alongside a fit to the median change in signal for each addition, where $R^2 = 0.86$.

2. Characteristics of Pristine Carbon Nanotube & Graphene Field Effect Transistors

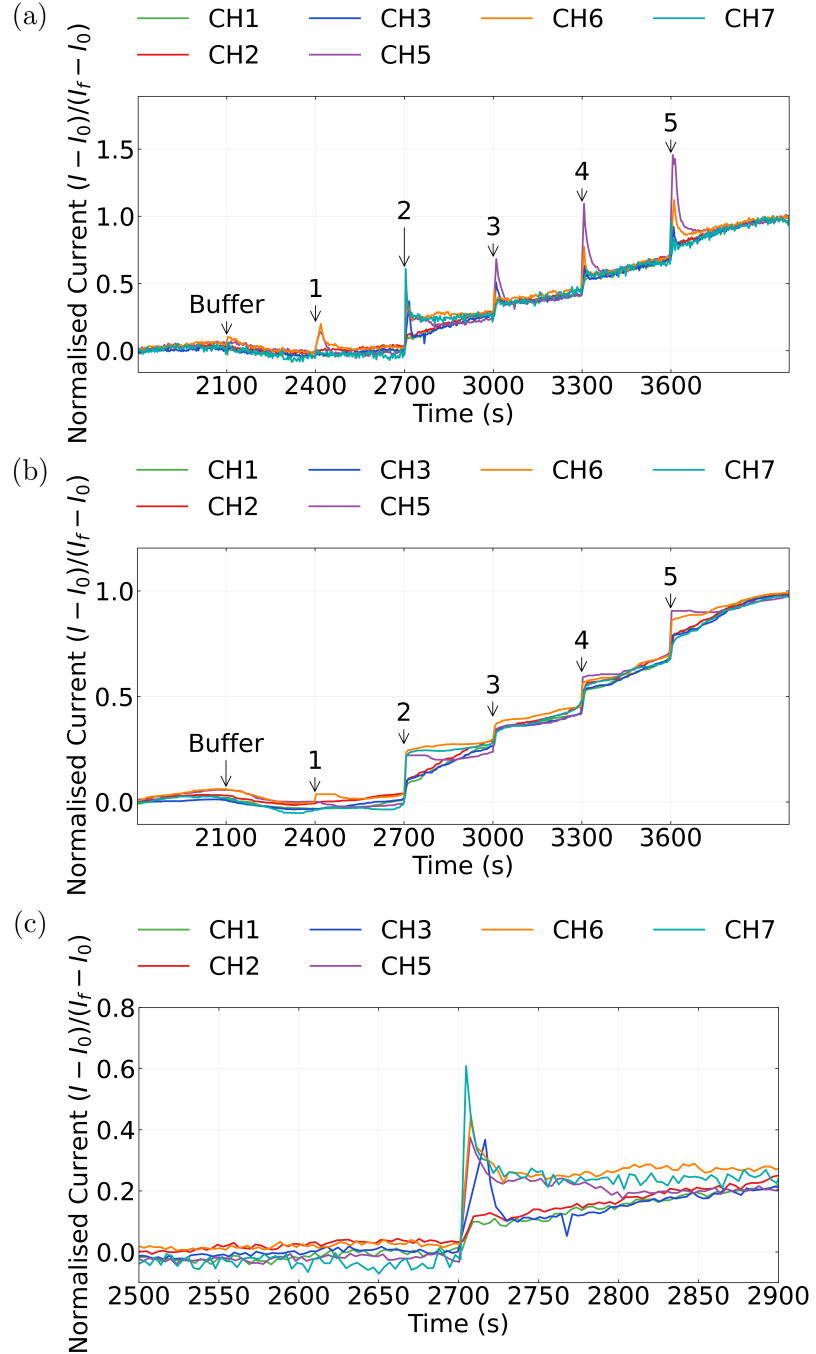


Figure 2.15.: The processed data shown in Figure 2.13 (b) and Figure 2.13 (c) is normalised to I_0 , but an alternative normalisation can more effectively filter out remaining drift present. This normalisation presents data relative to both I_0 and the final current reading I_f using the formula $(I - I_0)/(I_f - I_0)$. Using this normalisation, the data in Figure 2.13 (b) and Figure 2.13 (c) can be displayed instead as (a) and (b) respectively. (c) shows a magnified version of the step at addition 2 in (a).

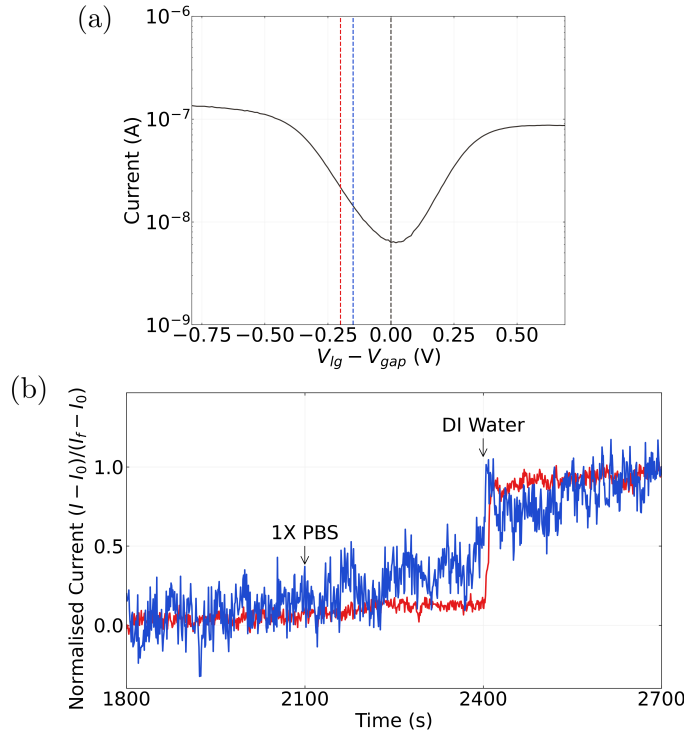


Figure 2.16.: The transfer characteristics of a single steam-deposited carbon nanotube field-effect transistor channel are shown in (a). V_{gap} is the gate voltage corresponding to the center of the transistor bandgap, found at the minimum of the characteristic curve. The signal-to-noise ratio of the channel response to a deionised water addition after a suitable control series is shown in (b). The blue current trace in (b) was performed gating the device 150 mV away from V_{gap} , while the red current was performed gating the device 200 mV away from V_{gap} .

A. Vapour System Hardware

Table A.1.: Major components used in construction of the vapour delivery system described in this thesis.

Description	Part No.	Manufacturer
Mass flow controller, 20 sccm full scale	GE50A-013201SBV020	MKS Instruments
Mass flow controller, 200 sccm full scale	GE50A-013202SBV020	MKS Instruments
Mass flow controller, 500 sccm full scale	FC-2901V	Tylan
Analogue flowmeter, 240 sccm max. flow	116261-30	Dwyer
Micro diaphragm pump	P200-B3C5V-35000	Xavitech
Analogue flow controller, for micro diaphragm pump	X3000450	Xavitech
10 mL Schott bottle	218010802	Duran
PTFE connection cap system	Z742273	Duran
Baseline VOC-TRAQ flow cell, purple	043-950	Ametek Mocon
Baseline VOC-TRAQ flow cell, red	043-951	Ametek Mocon
Humidity and temperature sensor	T9602-5-A	Telaire

B. Python Code for Data Analysis

B.1. Code Repository

The code used for general analysis of field-effect transistor devices in this thesis was written with Python 3.8.8. Contributors to the code used include Erica Cassie, Erica Happe, Marissa Dierkes and Leo Browning. The code is located on GitHub and the research group OneDrive, and is available on request.

B.2. Atomic Force Microscope Histogram Analysis

The purpose of this code is to analyse atomic force microscope (AFM) images of carbon nanotube networks in .xyz format taken using an atomic force microscope and processed in Gwyddion (see [?@sec-afm-characterisation](#)). It was originally designed by Erica Happe in Matlab, and adapted by Marissa Dierkes and myself for use in Python. The code imports the .xyz data and sorts it into bins 0.15 nm in size for processing. To perform skew-normal distribution fits, both *scipy.optimize.curve_fit* and *scipy.stats.skewnorm* modules are used in this code.

B.3. Raman Spectroscopy Analysis

The purpose of this code is to analyse a series of Raman spectra taken at different points on a single film (see [?@sec-raman-characterisation](#)). Data is imported in a series of tab-delimited text files, with the low wavenumber spectrum ($100\text{ cm}^{-1} - 650\text{ cm}^{-1}$) and high wavenumber spectrum ($1300\text{ cm}^{-1} - 1650\text{ cm}^{-1}$) imported in separate datafiles for each scan location.

B.4. Field-Effect Transistor Analysis

The purpose of this code is to analyse electrical measurements taken of field-effect transistor (FET) devices. Electrical measurements were either taken from the Keysight 4156C Semiconductor Parameter Analyser, National Instruments NI-PXIe or Keysight B1500A Semiconductor Device Analyser as discussed in [?@sec-electrical-characterisation](#);

B. Python Code for Data Analysis

the code is able to analyse data in .csv format taken from all three measurement setups. The main Python file in the code base consists of three related but independent modules: the first analyses and plots sensing data from the FET devices, the second analyses and plots transfer characteristics from channels across a device, and the third compares individual channel characteristics before and after a modification or after each individual modification in a series of modifications. The code base also features a separate config file and style sheet which govern the behaviour of the main code. The code base was designed collaboratively by myself and Erica Cassie over GitHub using the Sourcetree Git GUI.

References

- [1] Richard Glatz and Kelly Bailey-Hill. "Mimicking nature's noses: From receptor deorphaning to olfactory biosensing". In: *Progress in Neurobiology* 93 (2 Feb. 2011), pp. 270–296. ISSN: 0301-0082. DOI: 10.1016/J.PNEUROBIO.2010.11.004.
- [2] Oh Seok Kwon, Hyun Seok Song, Seon Joo Park, et al. "An Ultrasensitive, Selective, Multiplexed Superbioelectronic Nose That Mimics the Human Sense of Smell". In: *Nano Letters* 15 (10 Oct. 2015), pp. 6559–6567. ISSN: 15306992. DOI: 10.1021/ac s.nanolett.5b02286. URL: <https://pubs.acs.org/doi/full/10.1021/acs.nanolett.5b02286>.
- [3] Tran Thi Dung, Yunkwang Oh, Seon Jin Choi, et al. "Applications and Advances in Bioelectronic Noses for Odour Sensing". In: *Sensors 2018, Vol. 18, Page 103* 18 (1 Jan. 2018), p. 103. ISSN: 1424-8220. DOI: 10.3390/S18010103. URL: <https://www.mdpi.com/1424-8220/18/1/103>.
- [4] Chuntae Kim, Kyung Kwan Lee, Moon Sung Kang, et al. "Artificial olfactory sensor technology that mimics the olfactory mechanism: a comprehensive review". In: *Biomaterials Research* 2022 26:1 26 (1 Aug. 2022), pp. 1–13. ISSN: 2055-7124. DOI: 10.1186/S40824-022-00287-1. URL: <https://biomaterialsres.biomedcentral.com/articles/10.1186/s40824-022-00287-1>.
- [5] Douglas R. Kauffman and Alexander Star. "Electronically monitoring biological interactions with carbon nanotube field-effect transistors". In: *Chemical Society Reviews* 37 (6 May 2008), pp. 1197–1206. ISSN: 1460-4744. DOI: 10.1039/B709567H. URL: <https://pubs.rsc.org/en/content/articlehtml/2008/cs/b709567h%20https://pubs.rsc.org/en/content/articlelanding/2008/cs/b709567h>.
- [6] Niazul I. Khan, Mohammad Mousazadehkasin, Sujoy Ghosh, et al. "An integrated microfluidic platform for selective and real-time detection of thrombin biomarkers using a graphene FET". In: *Analyst* 145 (13 June 2020), pp. 4494–4503. ISSN: 13645528. DOI: 10.1039/d0an00251h. URL: <https://pubs.rsc.org/en/content/articlehtml/2020/an/d0an00251h%20https://pubs.rsc.org/en/content/articlelanding/2020/an/d0an00251h>.
- [7] Bajramshahe Shkodra, Mattia Petrelli, Martina Aurora Costa Angeli, et al. "Electrolyte-gated carbon nanotube field-effect transistor-based biosensors: Principles and applications". In: *Applied Physics Reviews* 8 (4 Dec. 2021), p. 41325. ISSN: 19319401. DOI: 10.1063/5.0058591. URL: [/aip/apr/article/8/4/041325/1076095/Electrolyte-gated-carbon-nanotube-field-effect](https://aip.org/aim/aim/8/4/041325/1076095/Electrolyte-gated-carbon-nanotube-field-effect).

References

- [8] Takahiro Arakawa, Takuma Suzuki, Masato Tsujii, et al. “Real-time monitoring of skin ethanol gas by a high-sensitivity gas phase biosensor (bio-sniffer) for the non-invasive evaluation of volatile blood compounds”. In: *Biosensors and Bioelectronics* 129 (Mar. 2019), pp. 245–253. ISSN: 0956-5663. DOI: 10.1016/J.BIOS.2018.09.070.
- [9] Heehong Yang, Daesan Kim, Jeongsu Kim, et al. “Nanodisc-Based Bioelectronic Nose Using Olfactory Receptor Produced in Escherichia coli for the Assessment of the Death-Associated Odor Cadaverine”. In: *ACS Nano* 11 (12 Dec. 2017), pp. 11847–11855. ISSN: 1936086X. DOI: 10.1021 / ACSNANO .7B04992. URL: <https://pubs.acs.org/doi/full/10.1021/acsnano.7b04992>.
- [10] Manki Son, Daesan Kim, Hwi Jin Ko, et al. “A portable and multiplexed bioelectronic sensor using human olfactory and taste receptors”. In: 87 (Jan. 2017), pp. 901–907. DOI: 10.1016/J.BIOS.2016.09.040. URL: <https://pubmed.ncbi.nlm.nih.gov/27664409/>.
- [11] Ariella Y. Moser, Wendy Y. Brown, Lewis A. Bizo, et al. “Biosecurity Dogs Detect Live Insects after Training with Odor-Proxy Training Aids: Scent Extract and Dead Specimens”. In: *Chemical Senses* 45 (3 Apr. 2020), pp. 179–186. ISSN: 14643553. DOI: 10.1093/CHEMSE/BJAA001. URL: <https://dx.doi.org/10.1093/chemse/bjaa001>.
- [12] Sang Hun Lee and Tai Hyun Park. “Recent advances in the development of bioelectronic nose”. In: *Biotechnology and Bioprocess Engineering* 15 (1 Feb. 2010), pp. 22–29. ISSN: 12268372. DOI: 10.1007/S12257-009-3077-1/METRICS. URL: <https://link.springer.com/article/10.1007/s12257-009-3077-1>.
- [13] Dongseok Moon, Yeon Kyung Cha, So ong Kim, et al. “FET-based nanobiosensors for the detection of smell and taste”. In: *Science China. Life sciences* 63 (8 Aug. 2020), pp. 1159–1167. ISSN: 1869-1889. DOI: 10.1007/S11427-019-1571-8. URL: <https://pubmed.ncbi.nlm.nih.gov/31974862/>.
- [14] Daigo Terutsuki, Hidefumi Mitsuno, Kohei Sato, et al. “Highly effective volatile organic compound dissolving strategy based on mist atomization for odorant biosensors”. In: *Analytica Chimica Acta* 1139 (Dec. 2020), pp. 178–188. ISSN: 0003-2670. DOI: 10.1016/J.ACA.2020.09.043.
- [15] Wyeonseok Yoon, Sang Hun Lee, Oh Seok Kwon, et al. “Polypyrrole nanotubes conjugated with human olfactory receptors: high-performance transducers for FET-type bioelectronic noses”. In: *Angewandte Chemie (International ed. in English)* 48 (15 Mar. 2009), pp. 2755–2758. ISSN: 1521-3773. DOI: 10.1002/ANIE.200805171. URL: <https://pubmed.ncbi.nlm.nih.gov/19274689/>.
- [16] Heehong Yang, Minju Lee, Daesan Kim, et al. “Bioelectronic Nose Using Olfactory Receptor-Embedded Nanodiscs”. In: *Methods in molecular biology (Clifton, N.J.)* 1820 (2018), pp. 239–249. ISSN: 1940-6029. DOI: 10.1007/978-1-4939-8609-5_18. URL: <https://pubmed.ncbi.nlm.nih.gov/29884950/>.

- [17] Elissa A. Hallem, Michael G. Ho, and John R. Carlson. “The molecular basis of odor coding in the *Drosophila* antenna”. In: *Cell* 117 (7 June 2004), pp. 965–979. ISSN: 00928674. DOI: 10.1016/j.cell.2004.05.012. URL: <https://pubmed.ncbi.nlm.nih.gov/15210116/>.
- [18] Renee Smart, Aidan Kiely, Morgan Beale, et al. “*Drosophila* odorant receptors are novel seven transmembrane domain proteins that can signal independently of heterotrimeric G proteins”. In: *Insect Biochemistry and Molecular Biology* 38 (8 Aug. 2008), pp. 770–780. ISSN: 09651748. DOI: 10.1016/J.IBMB.2008.05.002.
- [19] Dieter Wicher, Ronny Schäfer, René Bauernfeind, et al. “*Drosophila* odorant receptors are both ligand-gated and cyclic-nucleotide- activated cation channels”. In: *Nature* 452 (7190 Apr. 2008), pp. 1007–1011. ISSN: 14764687. DOI: 10.1038/NATURE06861.
- [20] Daniel Münch and C. Giovanni Galizia. “DoOR 2.0 - Comprehensive Mapping of *Drosophila melanogaster* Odorant Responses”. In: *Scientific Reports* 6 (Feb. 2016). ISSN: 20452322. DOI: 10.1038/SREP21841. URL: [/pmc/articles/PMC4766438/](https://pmc/articles/PMC4766438/)?report=abstract%20https://www.ncbi.nlm.nih.gov/pmc/articles/PMC4766438/
- [21] Jonathan D. Bohbot and Sefi Vernick. “The Emergence of Insect Odorant Receptor-Based Biosensors”. In: *Biosensors 2020, Vol. 10, Page 26* 10 (3 Mar. 2020), p. 26. ISSN: 2079-6374. DOI: 10.3390/BIOS10030026. URL: <https://www.mdpi.com/2079-6374/10/3/26>
- [22] Thanihaichelvan Murugathas, Han Yue Zheng, Damon Colbert, et al. “Biosensing with Insect Odorant Receptor Nanodiscs and Carbon Nanotube Field-Effect Transistors”. In: *ACS Applied Materials and Interfaces* 11 (9 Mar. 2019), pp. 9530–9538. ISSN: 19448252. DOI: 10.1021/ACSAM.8B19433. URL: <https://pubs.acs.org/doi/full/10.1021/acsam.8b19433>.
- [23] Thanihaichelvan Murugathas, Cyril Hamiaux, Damon Colbert, et al. “Evaluating insect odorant receptor display formats for biosensing using graphene field effect transistors”. In: *ACS Applied Electronic Materials* 2 (11 Nov. 2020), pp. 3610–3617. ISSN: 26376113. DOI: 10.1021/ACSAELM.0C00677. URL: <https://pubs.acs.org/doi/full/10.1021/acsaelm.0c00677>.
- [24] Tetsuya Yamada, Hirotaka Sugiura, Hisatoshi Mimura, et al. “Highly sensitive VOC detectors using insect olfactory receptors reconstituted into lipid bilayers”. In: *Science Advances* 7 (3 Jan. 2021). ISSN: 23752548. DOI: 10.1126/SCIADV.ABD2013.
- [25] Roshan Khadka, Nihan Aydemir, Colm Carraher, et al. “An ultrasensitive electrochemical impedance-based biosensor using insect odorant receptors to detect odorants”. In: *Biosensors and Bioelectronics* 126 (Feb. 2019), pp. 207–213. ISSN: 0956-5663. DOI: 10.1016/J.BIOS.2018.10.043.

References

- [26] Jamal Ahmed Cheema, Nihan Aydemir, Colm Carraher, et al. “Insect odorant receptor nanodiscs for sensitive and specific electrochemical detection of odorant compounds”. In: *Sensors and Actuators, B: Chemical* 329 (Feb. 2021). ISSN: 09254005. DOI: 10.1016/J.SNB.2020.129243.
- [27] H. Y. Zheng and N. O.V. Plank. “Facile fabrication of carbon nanotube network thin film transistors for device platforms”. In: *International Journal of Nanotechnology* 14 (1-6 2017), pp. 505–518. ISSN: 14757435. DOI: 10.1504/IJNT.2017.082473.
- [28] Thanihaichelvan Murugathas, Leo A. Browning, Marissa P. Dierkes, et al. “Data on liquid gated CNT network FETs on flexible substrates”. In: *Data in Brief* 21 (Dec. 2018), pp. 276–283. ISSN: 2352-3409. DOI: 10.1016/J.DIB.2018.09.093.
- [29] Thanihaichelvan Murugathas, Leo A. Browning, Marissa P. Dierkes, et al. “Metallic-semiconducting junctions create sensing hot-spots in carbon nanotube FET aptasensors near percolation”. In: *Biosensors and Bioelectronics* 130 (Apr. 2019), pp. 408–413. ISSN: 0956-5663. DOI: 10.1016/J.BIOS.2018.09.021.
- [30] Hong Phan T. Nguyen, Thanihaichelvan Murugathas, and Natalie O.V. Plank. “Comparison of Duplex and Quadruplex Folding Structure Adenosine Aptamers for Carbon Nanotube Field Effect Transistor Aptasensors”. In: *Nanomaterials (Basel, Switzerland)* 11 (9 Sept. 2021). ISSN: 2079-4991. DOI: 10.3390/NANO11092280. URL: <https://pubmed.ncbi.nlm.nih.gov/34578596/>.
- [31] Wim Wenseleers, Igor L. Vlasov, Etienne Goovaerts, et al. “Efficient Isolation and Solubilization of Pristine Single-Walled Nanotubes in Bile Salt Micelles”. In: *Advanced Functional Materials* 14 (11 Nov. 2004), pp. 1105–1112. ISSN: 1616-3028. DOI: 10.1002/ADFM.200400130. URL: <https://onlinelibrary.wiley.com/doi/full/10.1002/adfm.200400130%20https://onlinelibrary.wiley.com/doi/abs/10.1002/adfm.200400130%20https://onlinelibrary.wiley.com/doi/10.1002/adfm.200400130>.
- [32] Gildas Gavrel, Bruno Jousselme, Arianna Filoromo, et al. “Supramolecular Chemistry of Carbon Nanotubes”. In: (2013), pp. 95–126. DOI: 10.1007/128_2013_450.
- [33] Greg T. Hermanson. “Buckyballs, Fullerenes, and Carbon Nanotubes”. In: *Bioconjugate Techniques* (Jan. 2013), pp. 741–755. DOI: 10.1016/B978-0-12-382239-0.00016-9.
- [34] Maki Shimizu, Shunjiro Fujii, Takeshi Tanaka, et al. “Effects of surfactants on the electronic transport properties of thin-film transistors of single-wall carbon nanotubes”. In: *Journal of Physical Chemistry C* 117 (22 June 2013), pp. 11744–11749. ISSN: 19327455. DOI: 10.1021/JP3113254. URL: <https://pubs.acs.org/doi/full/10.1021/jp3113254>.
- [35] Antonello Di Crescenzo, Valeria Ettorre, and Antonella Fontana. “Non-covalent and reversible functionalization of carbon nanotubes”. In: *Beilstein Journal of Nanotechnology* 5 (1 2014), p. 1675. ISSN: 21904286. DOI: 10.3762/BJNANO.5.178. URL: [/pmc/articles/PMC4222398/](https://pmc/articles/PMC4222398/) %20https://www.ncbi.nlm.nih.gov/pmc/articles/PMC4222398/?report=abstract%20https://www.ncbi.nlm.nih.gov/pmc/articles/PMC4222398/.

- [36] Hee Bong Yang, Luke Neal, Elijah Earl Flores, et al. “Role and impact of surfactants in carbon nanotube dispersions and sorting”. In: *Journal of Surfactants and Detergents* 26 (5 Sept. 2023), pp. 607–622. ISSN: 1558-9293. DOI: 10.1002/JSD.12702. URL: <https://onlinelibrary.wiley.com/doi/full/10.1002/jsde.12702%20https://onlinelibrary.wiley.com/doi/abs/10.1002/jsde.12702%20https://aocs.onlinelibrary.wiley.com/doi/10.1002/jsde.12702>.
- [37] Melburne C. LeMieux, Mark Roberts, Soumendra Barman, et al. “Self-sorted, aligned nanotube networks for thin-film transistors”. In: *Science* 321 (5885 July 2008), pp. 101–104. ISSN: 00368075. DOI: 10.1126/SCIENCE.1156588. URL: <https://www.science.org>.
- [38] Chang Liu and Hui Ming Cheng. “Carbon nanotubes: controlled growth and application”. In: *Materials Today* 16 (1-2 Jan. 2013), pp. 19–28. ISSN: 1369-7021. DOI: 10.1016/J.MATTOD.2013.01.019.
- [39] Dusan Vobornik, Maohui Chen, Shan Zou, et al. “Measuring the Diameter of Single-Wall Carbon Nanotubes Using AFM”. In: *Nanomaterials* 13 (3 Feb. 2023), p. 477. ISSN: 20794991. DOI: 10.3390/NANO13030477. URL: <https://www.mdpi.com/2079-4991/13/3/477>.
- [40] Adelchi Azzalini and Antonella Capitanio. “The skew-normal distribution: probability”. In: Cambridge University Press, Dec. 2013, pp. 24–56. ISBN: 9781139248891. DOI: 10.1017/CBO9781139248891. URL: <https://www.cambridge.org/core/books/skewnormal-and-related-families/4B9A3CD9D58EB6022FC1D21E1E08A10E>.
- [41] Matěj Velický, Adam J Cooper, Peter S Toth, et al. “Mechanical stability of substrate-bound graphene in contact with aqueous solutions”. In: *2D Materials* 2 (2 May 2015), p. 024011. ISSN: 2053-1583. DOI: 10.1088/2053-1583/2/2/024011. URL: <https://iopscience.iop.org/article/10.1088/2053-1583/2/2/024011%20https://iopscience.iop.org/article/10.1088/2053-1583/2/2/024011/meta>.
- [42] Erin E. Christensen, Mitesh Amin, Trevor M. Tumiel, et al. “Localized Charge on Surfactant-Wrapped Single-Walled Carbon Nanotubes”. In: *Journal of Physical Chemistry Letters* 13 (46 Nov. 2022), pp. 10705–10712. ISSN: 19487185. DOI: 10.1021/ACS.JPCLETT.2C02650. URL: <https://pubs.acs.org/doi/full/10.1021/acs.jpclett.2c02650>.
- [43] E. Ukrainstsev, A. Kromka, H. Kozak, et al. “Artifacts in Atomic Force Microscopy of Biological Samples”. In: InTech, Mar. 2012. DOI: 10.5772/36203.
- [44] R. L. Graham, B. D. Lubachevsky, K. J. Nurmela, et al. “Dense packings of congruent circles in a circle”. In: *Discrete Mathematics* 181 (1-3 Feb. 1998), pp. 139–154. ISSN: 0012-365X. DOI: 10.1016/S0012-365X(97)00050-2.
- [45] Eckard Specht. *The best known packings of equal circles in a circle*. URL: <http://hydra.nat.uni-magdeburg.de/packing/cci/cci.html>.
- [46] Yulia V Marchenko and Marc G Genton. “A suite of commands for fitting the skew-normal and skew-t models”. In: *The Stata Journal* 10 (4 2010), pp. 507–539.

References

- [47] Alexander A. Kane, Alexandra C. Ford, April Nissen, et al. “Etching of surfactant from solution-processed, type-separated carbon nanotubes and impact on device behavior”. In: *ACS Nano* 8 (3 Mar. 2014), pp. 2477–2485. ISSN: 1936086X. DOI: 10.1021/NN406065T. URL: <https://pubs.acs.org/doi/full/10.1021/nn406065t>.
- [48] Chris J. Barnett, Cathren E. Gowenlock, Kathryn Welsby, et al. “Spatial and Contamination-Dependent Electrical Properties of Carbon Nanotubes”. In: *Nano letters* 18 (2 Feb. 2018), pp. 695–700. ISSN: 1530-6992. DOI: 10.1021/ACS.NANOLETT.7B03390. URL: <https://pubmed.ncbi.nlm.nih.gov/29257695/>.
- [49] Millie S. Dresselhaus, G. Dresselhaus, R. Saito, et al. “Raman spectroscopy of carbon nanotubes”. In: *Physics Reports* 409 (2 Mar. 2005), pp. 47–99. ISSN: 0370-1573. DOI: 10.1016/J.PHYSREP.2004.10.006.
- [50] Benjamin King and Balaji Panchapakesan. “Vacuum filtration based formation of liquid crystal films of semiconducting carbon nanotubes and high performance transistor devices”. In: *Nanotechnology* 25 (17 Apr. 2014), p. 175201. ISSN: 0957-4484. DOI: 10.1088/0957-4484/25/17/175201. URL: [https://iopscience.iop.org/article/10.1088/0957-4484/25/17/175201/meta](https://iopscience.iop.org/article/10.1088/0957-4484/25/17/175201%20https://iopscience.iop.org/article/10.1088/0957-4484/25/17/175201/meta).
- [51] M. Świniarski, A. Dużyńska, A. P. Gertych, et al. “Determination of the electronic transport in type separated carbon nanotubes thin films doped with gold nanocrystals”. In: *Scientific Reports* 2021 11:1 11 (1 Aug. 2021), pp. 1–7. ISSN: 2045-2322. DOI: 10.1038/s41598-021-96307-6. URL: <https://www.nature.com/articles/s41598-021-96307-6>.
- [52] Jeff L. Blackburn, Chaiwat Engtrakul, Timothy J. McDonald, et al. “Effects of Surfactant and Boron Doping on the BWF Feature in the Raman Spectrum of Single-Wall Carbon Nanotube Aqueous Dispersions”. In: *The Journal of Physical Chemistry B* 110 (50 Dec. 2006), pp. 25551–25558. ISSN: 1520-6106. DOI: 10.1021/jp065287m.
- [53] David C. Stone. “Application of median filtering to noisy data”. In: 73 (10 Oct. 2011), pp. 1573–1581. ISSN: 0008-4042. DOI: 10.1139/V95-195. URL: <https://cdnciencepub.com/doi/10.1139/v95-195>.
- [54] I. Heller, S. Chattoor, J. Männik, et al. “Comparing the weak and strong gate-coupling regimes for nanotube and graphene transistors”. In: *physica status solidi (RRL) – Rapid Research Letters* 3 (6 Sept. 2009), pp. 190–192. ISSN: 1862-6270. DOI: 10.1002/PSSR.200903157. URL: <https://onlinelibrary.wiley.com/doi/full/10.1002/pssr.200903157%20https://onlinelibrary.wiley.com/doi/abs/10.1002/pssr.200903157%20https://onlinelibrary.wiley.com/doi/10.1002/pssr.200903157>.
- [55] Iddo Heller, Sohail Chattoor, Jaan Männik, et al. “Influence of electrolyte composition on liquid-gated carbon nanotube and graphene transistors”. In: *Journal of the American Chemical Society* 132 (48 Dec. 2010), pp. 17149–17156. ISSN: 00027863. DOI: 10.1021/JA104850N. URL: <https://pubs.acs.org/doi/full/10.1021/ja104850n>.

- [56] Fengnian Xia, Damon B. Farmer, Yu Ming Lin, et al. “Graphene field-effect transistors with high on/off current ratio and large transport band gap at room temperature”. In: *Nano Letters* 10 (2 Feb. 2010), pp. 715–718. ISSN: 15306984. DOI: 10.1021/NL9039636. URL: <https://pubs.acs.org/doi/full/10.1021/nl9039636>.
- [57] Dmitry Kireev, Max Brambach, Silke Seyock, et al. “Graphene transistors for interfacing with cells: towards a deeper understanding of liquid gating and sensitivity”. In: *Scientific Reports* 2017 7:1 7 (1 July 2017), pp. 1–12. ISSN: 2045-2322. DOI: 10.1038/s41598-017-06906-5. URL: <https://www.nature.com/articles/s41598-017-06906-5>.
- [58] Antonio Di Bartolomeo, Filippo Giubileo, Salvatore Santandrea, et al. “Charge transfer and partial pinning at the contacts as the origin of a double dip in the transfer characteristics of graphene-based field-effect transistors”. In: *Nanotechnology* 22 (27 May 2011), p. 275702. ISSN: 0957-4484. DOI: 10.1088/0957-4484/22/27/275702. URL: <https://iopscience.iop.org/article/10.1088/0957-4484/22/27/275702>. <https://iopscience.iop.org/article/10.1088/0957-4484/22/27/275702/meta>.
- [59] Zengguang Cheng, Qiaoyu Zhou, Chenxuan Wang, et al. “Toward intrinsic graphene surfaces: A systematic study on thermal annealing and wet-chemical treatment of SiO₂-supported graphene devices”. In: *Nano Letters* 11 (2 Feb. 2011), pp. 767–771. ISSN: 15306984. DOI: 10.1021/NL103977D. URL: <https://pubs.acs.org/doi/full/10.1021/nl103977d>.
- [60] Dong Wook Shin, Hyun Myoung Lee, Seong Man Yu, et al. “A facile route to recover intrinsic graphene over large scale”. In: *ACS Nano* 6 (9 Sept. 2012), pp. 7781–7788. ISSN: 19360851. DOI: 10.1021/NN3017603. URL: <https://pubs.acs.org/doi/full/10.1021/nn3017603>.
- [61] Y. Bargaoui, M. Troudi, P. Bondavalli, et al. “Gate bias stress effect in single-walled carbon nanotubes field-effect-transistors”. In: *Diamond and Related Materials* 84 (Apr. 2018), pp. 62–65. ISSN: 0925-9635. DOI: 10.1016/J.DIAMOND.2018.03.011.
- [62] Steven G. Noyce, James L. Doherty, Zhihui Cheng, et al. “Electronic Stability of Carbon Nanotube Transistors under Long-Term Bias Stress”. In: *Nano Letters* 19 (3 Mar. 2019), pp. 1460–1466. ISSN: 15306992. DOI: 10.1021/ACS.NANOLETT.8B03986. URL: <https://pubs.acs.org/doi/full/10.1021/acs.nanolett.8b03986>.
- [63] Song-ang Peng, Zhi Jin, Dayong Zhang, et al. “How Do Contact and Channel Contribute to the Dirac Points in Graphene Field-Effect Transistors?” In: *Advanced Electronic Materials* 4 (8 Aug. 2018), p. 1800158. ISSN: 2199-160X. DOI: 10.1002/AELM.201800158. URL: <https://onlinelibrary.wiley.com/doi/full/10.1002/aelm.201800158>. <https://onlinelibrary.wiley.com/doi/10.1002/aelm.201800158>.
- [64] Joon Sung Lee, Sunmin Ryu, Kwonjae Yoo, et al. “Origin of gate hysteresis in carbon nanotube field-effect transistors”. In: *Journal of Physical Chemistry C* 111 (34 Aug. 2007), pp. 12504–12507. ISSN: 19327447. DOI: 10.1021/JP074692Q. URL: <https://pubs.acs.org/doi/full/10.1021/jp074692q>.

References

- [65] Sang Won Lee, Si Young Lee, Seong Chu Lim, et al. “Positive gate bias stress instability of carbon nanotube thin film transistors”. In: *Applied Physics Letters* 101 (5 July 2012). ISSN: 00036951. DOI: 10.1063/1.4740084/111432. URL: [/aip/apl/article/101/5/053504/111432/Positive-gate-bias-stress-instability-of-carbon](https://aip.org/article/101/5/053504/111432/Positive-gate-bias-stress-instability-of-carbon).
- [66] Tae Jun Ha, Daisuke Kiriya, Kevin Chen, et al. “Highly stable hysteresis-free carbon nanotube thin-film transistors by fluorocarbon polymer encapsulation”. In: *ACS Applied Materials and Interfaces* 6 (11 June 2014), pp. 8441–8446. ISSN: 19448252. DOI: 10.1021/AM5013326. URL: <https://pubs.acs.org/doi/full/10.1021/am5013326>.
- [67] Nima Rouhi, Dheeraj Jain, Katayoun Zand, et al. “Fundamental limits on the mobility of nanotube-based semiconducting inks”. In: *Advanced Materials* 23 (1 Jan. 2011), pp. 94–99. ISSN: 09359648. DOI: 10.1002/ADMA.201003281.
- [68] Zhongyu Li, Mengmeng Xiao, Chuanhong Jin, et al. “Toward the Commercialization of Carbon Nanotube Field Effect Transistor Biosensors”. In: *Biosensors 2023, Vol. 13, Page 326* 13 (3 Feb. 2023), p. 326. ISSN: 2079-6374. DOI: 10.3390/BIOS13030326. URL: <https://www.mdpi.com/2079-6374/13/3/326> <https://www.mdpi.com/2079-6374/13/3/326>.
- [69] Woong Kim, Ali Javey, Ophir Vermesh, et al. “Hysteresis Caused by Water Molecules in Carbon Nanotube Field-Effect Transistors”. In: *NANO LETTERS* 3 (2 2003), pp. 193–198. DOI: 10.1021/nl0259232.
- [70] Aaron D. Franklin, George S. Tulevski, Shu Jen Han, et al. “Variability in carbon nanotube transistors: Improving device-to-device consistency”. In: *ACS Nano* 6 (2 Feb. 2012), pp. 1109–1115. ISSN: 19360851. DOI: 10.1021/NN203516Z. URL: <https://pubs.acs.org/doi/full/10.1021/nn203516z>.
- [71] Helene Conseil, Morten S. Jellesen, and Rajan Ambat. “Experimental study of water absorption of electronic components and internal local temperature and humidity into electronic enclosure”. In: *Proceedings of the 16th Electronics Packaging Technology Conference, EPTC 2014* (Jan. 2014), pp. 355–359. DOI: 10.1109/EPTC.2014.7028356.
- [72] Iddo Heller, Jaan Männik, Serge G. Lemay, et al. “Optimizing the signal-to-noise ratio for biosensing with carbon nanotube transistors”. In: *Nano Letters* 9 (1 Jan. 2009), pp. 377–382. ISSN: 15306984. DOI: 10.1021/NL8031636. URL: <https://pubs.acs.org/doi/full/10.1021/nl8031636>.
- [73] Woo Jong Yu, Un Jeong Kim, Bo Ram Kang, et al. “Adaptive Logic Circuits with Doping-Free Ambipolar Carbon Nanotube Transistors”. In: *NANO LETTERS* 9 (4 2009), pp. 1401–1405. DOI: 10.1021/nl803066v. URL: <https://pubs.acs.org/sharingguidelines>.
- [74] Vladimir Derenskyi, Widiantha Gomulya, Jorge Mario Salazar Rios, et al. “Carbon Nanotube Network Ambipolar Field-Effect Transistors with 108 On/Off Ratio”. In: *Advanced Materials* 26 (34 Sept. 2014), pp. 5969–5975. ISSN: 15214095. DOI: 10.1002/ADMA.201401395.

- [75] Faris M. Albarghouthi, Nicholas X. Williams, James L. Doherty, et al. "Passivation Strategies for Enhancing Solution-Gated Carbon Nanotube Field-Effect Transistor Biosensing Performance and Stability in Ionic Solutions". In: *ACS Applied Nano Materials* 5 (10 Oct. 2022), pp. 15865–15874. ISSN: 25740970. DOI: 10.1021/ACS ANM.2C04098. URL: <https://doi.org/10.1021/acsanm.2c04098>.
- [76] Eric Pop, Sumit Dutta, David Estrada, et al. "Avalanche, Joule breakdown and hysteresis in carbon nanotube transistors". In: *IEEE International Reliability Physics Symposium Proceedings* (2009), pp. 405–408. ISSN: 15417026. DOI: 10.1109/IRPS.2009.5173287.
- [77] Jana Zaumseil. "Single-walled carbon nanotube networks for flexible and printed electronics". In: *Semiconductor Science and Technology* 30 (7 June 2015), p. 074001. ISSN: 0268-1242. DOI: 10.1088/0268-1242/30/7/074001. URL: <https://iopscience.iop.org/article/10.1088/0268-1242/30/7/074001%20https://iopscience.iop.org/article/10.1088/0268-1242/30/7/074001/meta>.
- [78] Xuan P A Gao, Gengfeng Zheng, and Charles M Lieber. "Subthreshold Regime has the Optimal Sensitivity for Nanowire FET Biosensors". In: (2010). DOI: 10.1021/nl9034219. URL: <https://pubs.acs.org/sharingguidelines>.
- [79] Donghun Kang, Noejung Park, Ju Hye Ko, et al. "Oxygen-induced p-type doping of a long individual single-walled carbon nanotube". In: *Nanotechnology* 16 (8 May 2005), p. 1048. ISSN: 0957-4484. DOI: 10.1088/0957-4484/16/8/008. URL: <https://iopscience.iop.org/article/10.1088/0957-4484/16/8/008%20https://iopscience.iop.org/article/10.1088/0957-4484/16/8/008/meta>.
- [80] Iddo Heller, Anne M. Janssens, Jaan Männik, et al. "Identifying the mechanism of biosensing with carbon nanotube transistors". In: *Nano Letters* 8 (2 Feb. 2008), pp. 591–595. ISSN: 15306984. DOI: 10.1021/NL072996I. URL: <https://pubs.acs.org/doi/full/10.1021/nl072996i>.
- [81] Yoshiyuki Nonoguchi, Atsushi Tani, Tomoko Murayama, et al. "Surfactant-driven Amphoteric Doping of Carbon Nanotubes". In: *Chemistry - An Asian Journal* 13 (24 Dec. 2018), pp. 3942–3946. ISSN: 1861471X. DOI: 10.1002/ASIA.201801490.
- [82] H. Lin and S. Tiwari. "Localized charge trapping due to adsorption in nanotube field-effect transistor and its field-mediated transport". In: *Applied Physics Letters* 89 (7 Aug. 2006), p. 73507. ISSN: 00036951. DOI: 10.1063/1.2337104. URL: [/aip/a pl/article/89/7/073507/332595/Localized-charge-trapping-due-to-adsorption-in](https://aip.org/article/89/7/073507/332595/Localized-charge-trapping-due-to-adsorption-in).

